Astronomy & Astrophysics manuscript no. PDR30Dor
March 14, 2016
©ESO 2016

arXiv:1603.03573v1 [astro-ph.GA] 11 Mar 2016

A milestone toward understanding PDR properties in the extreme environment of LMC-30Dor

M. Chevance[1,2], S. C. Madden[1], V. Lebouteiller[1], B. Godard[3], D. Cormier[4], F. Galliano[1], S. Hony[4], R. Indebetouw[5,6], J. Le Bourlot[3], M.-Y. Lee[1], F. Le Petit[3], E. Pellegrini[4], E. Roueff[3], and R. Wu[7]

[1] Laboratoire AIM, CEA/DSM - CNRS - Université Paris Diderot, IRFU/Service d'Astrophysique, CEA Saclay, 91191 Gif-sur-Yvette, France. e-mail: melanie.chevance@cea.fr
[2] Université Paris Diderot, Sorbonne Paris Cité, F-75205 Paris, France
[3] LERMA, Observatoire de Paris & CNRS, 5 place Jules Janssen, 92190 Meudon, France
[4] Institut für theoretische Astrophysik, Zentrum für Astronomie der Universität Heidelberg, Albert-Ueberle Str. 2, D-69120 Heidelberg, Germany
[5] Department of Astronomy, University of Virginia, PO Box 3818, Charlottesville, VA 22903, USA
[6] National Radio Astronomical Observatory, Charlottesville, VA 22904, USA
[7] Department of Astronomy, Graduate School of Science, The University of Tokyo, Bunkyo-ku, Tokyo 113-0033, Japan

Received ; accepted

ABSTRACT

Context. More complete knowledge of galaxy evolution requires understanding the process of star formation and interaction between the interstellar radiation field and the interstellar medium (ISM) in galactic environments traversing a wide range of physical parameter space. Here we focus on the impact of massive star formation on the surrounding low metallicity ISM in 30 Doradus in the Large Magellanic Cloud (LMC). A low metal abundance, as is the case of some galaxies of the early universe, results in less ultra-violet (UV) shielding for the formation of the molecular gas necessary for star formation to proceed. The half-solar metallicity gas in this region is strongly irradiated by the super star cluster R136, making it an ideal laboratory to study the structure of the ISM in an extreme environment.

Aims. Our goal is to construct a comprehensive, self-consistent picture of the density, radiation field, and ISM structure in the most active star-forming region in the LMC, 30 Doradus. Our *spatially* resolved study investigates the gas heating and cooling mechanisms, particularly in the photo-dissociation regions where the chemistry and thermal balance are regulated by far-ultraviolet photons (6 eV< hν <13.6 eV).

Methods. We present *Herschel* observations of far-infrared fine-structure lines obtained with PACS and SPIRE/FTS. We have combined atomic fine-structure lines from *Herschel* and *Spitzer* observations with ground-based CO data to provide diagnostics on the properties and the structure of the gas by modeling it with the Meudon PDR code. For each tracer we estimate the possible contamination from the ionized gas in order to isolate the PDR component alone. We derive the spatial distribution of the radiation field, the pressure, the size, and the filling factor of the photodissociated gas and molecular clouds.

Results. We find a range of pressure of $\sim 10^5 - 1.7\times10^6$ cm^{-3} K and a range of incident radiation field $G_{UV}\sim 10^2 - 2.5\times10^4$ through PDR modeling. Assuming a plane-parallel geometry and a uniform medium, we find a total extinction A_V^{max} of 1 – 3 mag , which correspond to a PDR cloud size of 0.2 to 3pc, with small CO depth scale of 0.06 to 0.5pc. At least 90% of the [C II] originates in PDRs in this region, while a significant fraction of the L_{FIR} (up to 70% in some places) can be associated with an ionized gas component. The high [O III]/[C II] ratio (2 to 60) throughout the observed map, correlated with the filling factor, reveals the porosity of the ISM in this region, traversed by hard UV photons, surrounding small PDR clumps. We also determine the three dimensional structure of the gas, showing that the clouds are distributed 20 to 80 pc away from the main ionizing cluster, R136.

1. Introduction

Galaxy evolution is dictated by progressive chemical enrichment which is mostly achieved through a succession of star formation episodes. The effect of metal enrichment on what we observe to be the star formation and interstellar medium (ISM) properties remains elusive despite circumstantial evidence. For example, reduced metallicity is expected to have important consequences on the chemistry and the subsequent heating and cooling mechanisms of the gas and dust, directly affecting the transition of the atomic to molecular phase. In low metallicity environments, the transition between C^+/C/CO can be shifted further into the cloud in physical scale, leaving a relatively larger photodissociation region (PDR) and a smaller CO core, compared to more metal-rich environments, such as the Milky Way (Kaufman et al. 1999). This effect on the molecular cloud structure manifests itself in an observed low CO luminosity in dwarf galaxies (e.g. Cormier et al. 2014; Schruba et al. 2012) and requires a higher CO-to-H_2 conversion factor, the X_{CO} factor (Schruba et al. 2012; Bolatto et al. 2013). It could also possibly be explained by a higher star formation efficiency.

Dwarf galaxies in our local universe are the closest environments we can explore in detail to witness the interplay between star formation and ISM under low metallicity conditions. Large surveys probing the cooling of dwarf galaxies have been possible for the first time with the *Herschel* Space Observatory (Pilbratt et al. 2010 ; e.g. the Dwarf Galaxy Survey, DGS ; Madden et al. 2013). Recent studies taking advantage of the *Herschel* sensitivity, have modeled the dust and gas properties of a wide range of low metallicity galaxies on integrated galaxy scales (e.g. Rémy-Ruyer et al. 2013, 2014; Rémy-Ruyer et al. 2015; Cormier et al. 2012, 2015; Cigan et al. 2015) and find prominent differences between metal-rich and metal poor galaxies. For example, from far-

infrared (FIR) line ratios, Cormier et al. (2015) have determined that radiation fields over global galaxy scales are harder in star-forming dwarf galaxies, compared to more metal-rich galaxies. Furthermore, the filling factor of the ionized gas appears larger relatively to the neutral gas. As a consequence of the low metallicity and low extinction in dwarf galaxies, it is possible that a significant fraction of the molecular gas is not traced by CO, but may be residing in the C^+ or C^0- emitting region for example (referred to as the "dark gas" in Wolfire et al. 2010), quantified in low metallicity environments using C^+ by Poglitsch et al. (1995) and Madden et al. (1997) and more recently in our Galaxy by Langer et al. (2014) and Pineda et al. (2014).

The Large Magellanic Cloud is our closest low metallicity galaxy neighbor (1/2 $Z_\odot$, Rolleston et al. 2002; Pagel 2003; 50 kpc, Walker 2012) allowing us to zoom into the ISM at the spatial resolution of $\sim 12''$ ($\sim$ 3 pc) with *Herschel*. We focus on 30 Doradus (hereafter "30Dor"), which is the most prominent star-forming region in the LMC and provides the best laboratory to study the impact of a super star cluster (SSC) on the ISM. The primary ultraviolet radiation source illuminating this region is the SSC R136, containing 39 O3 stars (Hunter 1999), often considered to be the most extreme star-forming region in the Local Group. The lower dust abundance of the LMC allows for deep penetration of the ionizing radiation, creating extended PDR regions and a more porous environment channeling the UV photons. ALMA observations from Indebetouw et al. (2013) have revealed the clumpy structure of the molecular gas in 30Dor, showing small ^{12}CO filaments and clumps ($\lesssim$ 1 pc) covering about 15% of their map. We examine the PDR conditions in the neutral atomic gas using mainly [C II] and [O I] observed by *Herschel* in this region to unveil the spatial distribution of the radiation field and the structure of the photodissociated gas and molecular clouds. The fraction of CO-dark gas based on this detailed study will be quantified in a following study (Chevance et al. in prep, hereafter paper II).

Observations of the ionized gas were conducted with *Spitzer* and studied by Indebetouw et al. (2009). They showed in particular that photoionization dominates the ionization structure of the gas over shocks in the H II region around R136. A study of the fine structure lines of C^+ and O^0 in 30Dor has been previously carried out by Poglitsch et al. (1995), with the Kuiper Airborne Observatory (KAO), at a resolution of ~55″ ($\sim$ 13 pc). They found that a highly fragmented structure with high density clouds ($n = 10^3 - 10^4$ cm^{-3}), of low relative beam filling-factor of CO compared to the PDR (4% of the clumps volume), bathed in ionized gas could explain the observed ratio [C II]/CO (ten times higher than the Galactic value). Moreover, most of the molecular gas may be present in the PDR, and faint in CO. Now, the PACS observations provide better spatial resolution than the KAO data and include other important tracers, with an improved signal-to-noise ratio. Pineda et al. (2012) have investigated the CO and [C I] emission observed with the NANTEN2 4-m telescope in a 26″ beam, combined with the KAO observations of [C II] in 30Dor and found likewise a very clumpy medium.

We present spectroscopic data of 30Dor in Section 2. Section 3 describes the observed maps and some preliminary results. In Section 4 we use PDR models to determine the physical parameters of the gas in PDR and we study the impact of metallicity and geometry on these parameters. We discuss our results and build a comprehensive 3D picture of the region in Section 5. Key results and conclusions are summarized in Section 6.

2. Observations and data preparation

2.1. *Herschel* PACS spectroscopy

We have mapped five fine structure lines, [C II] 158 μm, [N II] 122 μm, [O I] 63 μm, [O I] 145 μm and [O III] 88 μm using the Photodetector Array Camera and Spectrometer (PACS, Poglitsch et al. 2010) towards 30Dor. Properties of these lines are presented in Table 1 and the maps can be seen in Figure 1. These observations, described in Madden et al. (2013), are part of the *Herschel* key program, SHINING (P.I. E. Sturm). We also used two additional pointings east of R136, which were observed by Indebetouw et al (OT2) in [C II], [O I] 63 μm, [N II] 122 μm and [O III] 88 μm. The details of the observations are shown in Appendix A.

The PACS array is composed of 5×5 spatial pixels (or *spaxels*) of 9.4″ covering a total field of view of 47″. The fine structure lines [O I] 63 μm, [O III] 88 μm, [N II] 122 μm, [O I] 145 μm and [C II] were mapped with respectively 25, 25, 4, 11 and 31 raster positions, covering approximately a $4' \times 5'$ region (56 pc×70 pc). The observations were done in unchopped mode. The beam size is 9.5" at 60 μm, and 12" at 160 μm (PACS Observer's Manual 2011).

We refer to Cormier et al. (2015) for the full description of the PACS observations and data reduction, and we summarize here some of the main steps. The data were reduced with the *Herschel* Interactive Processing Environment (HIPE) v12.0.0 (Ott 2010) from Level 0 to Level 1. The Level 1 cubes, calibrated in flux and wavelength, are then exported and processed with PACSman v3.61 (Lebouteiller et al. 2012) to fit the lines and create the individual maps. Each spectrum is fitted with a second order polynomial for the baseline and a Gaussian for the line. Finally the individual rasters are projected onto a common grid of $3'' \times 3''$ pixels (0.72×0.72 pc) to reconstruct the final maps. Uncertainties on the fit and on the projection are estimated using a Monte-Carlo simulation. All of the lines are well detected everywhere in the map (Fig. 1). The weakest line, [N II] 122 μm has a signal-to-noise ratio (SNR) between 5 and 30 for most of the mapped area. The emission line [O I] 145 μm has a SNR between 7 and 90 and the SNR is above 10 for all of the other lines.

The observed intensities match well those detected with the Kuiper Airborne Observatory by Poglitsch et al. (1995) with a lower spatial resolution (55″ for [C II] and [O I] 145 μm and 22″ for [O I] 63 μm). For example they found a maximum [C II] intensity of 10^{-3} erg s^{-1}cm^{-2}sr^{-1}, and we measure a maximum intensity of 1.1×10^{-3} erg s^{-1}cm^{-2}sr^{-1} on PACS data convolved to the same resolution. They are also similar to the [C II] intensities measured by Requena-Torres (in prep) using the GREAT instrument on *SOFIA*.

2.2. *Herschel* SPIRE spectroscopy

The SPIRE instrument includes an Imaging Fourier Transform Spectrometer (FTS) covering the wavelength ranges 194–324 and 316–672 μm (SPIRE Short Wavelength SSW and SPIRE Long Wavelength SLW arrays respectively). 30Dor was observed with the SPIRE FTS in the high spectral resolution ($\Delta\nu \sim$ 1.2 GHz), intermediate spatial sampling mode. In the intermediate spatial sampling mode, SLW and SSW are moved between four jiggling positions with a spacing of ~28″ and ~16″ respectively. The observations were performed on January 8, 2013 (observation IDs: 1342219550, 1342257932 and 1342262908) with a total integration time of $\sim$ 15400s.

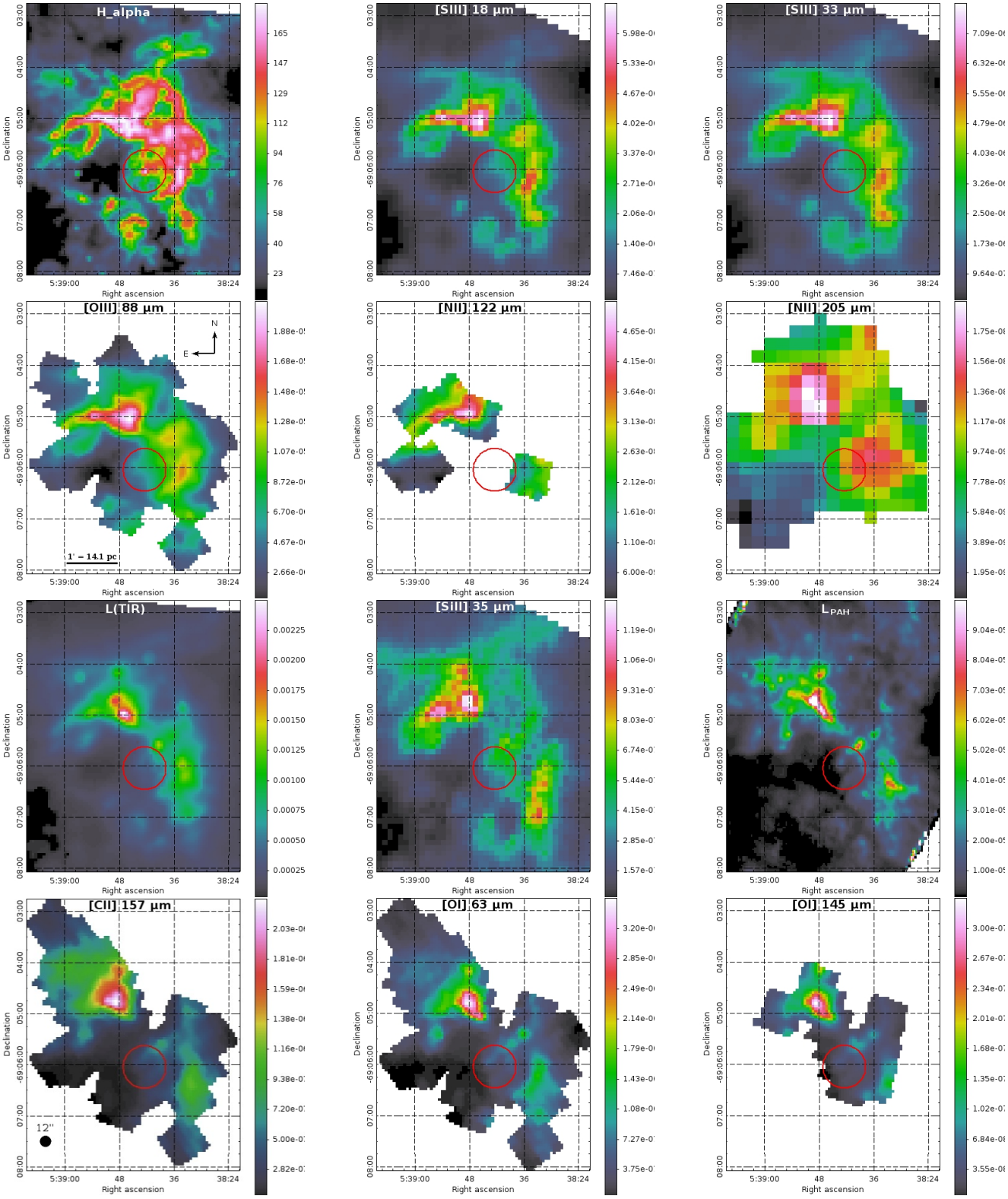

Fig. 1. PDR and ionized gas line emission from *Herschel* (PACS and SPIRE/FTS) and *Spitzer*/IRS observations of the 30Dor region in W m^{-2} sr^{-1}.The maps are shown at their original spatial resolution. The L_{TIR} map is the total far-infrared luminosity integrated between 3-1000 μm from our SED modeling. The red circle represents the location of the R136 cluster. Table 1 and Section 2 describe these observations in detail.

Table 1. Properties of lines and observations.

Instrument	Transition	λ (μm)	FWHM (arcsec)	Ionization energy (eV)	$n_{crit}{}^{a}$ (cm^{-3})
PACS	[O I] $^3P_1 - ^3P_2$	63.2	9.5	–	4.7×10^5 [H]
	[O I] $^3P_0 - ^3P_1$	145.5	11.0	–	9.5×10^4 [H]
	[O III] $^3P_1 - ^3P_0$	88.3	9.5	35.1	510 [e]
	[C II] $^2P_{3/2} - ^2P_{1/2}$	157.7	11.6	11.3	2.8×10^3 [H], 50 [e]
	[N II] $^3P_2 - ^3P_1$	121.8	9.9	14.5	310 [e]
SPIRE/FTS	[N II] $^3P_1 - ^3P_0$	205.3	16.6	14.5	48 [e]
	[C I] $^3P_2 - ^3P_1$	370.4	36.2	–	1.2×10^3 [H_2]
	[C I] $^3P_1 - ^3P_0$	609.7	38.6	–	4.7×10^3 [H_2]
Spitzer/IRS[b]	[S III] $^3P_2 - ^3P_1$	18.7	4.9	23.3	2×10^4 [e]
	[S III] $^3P_1 - ^3P_0$	33.5	8.9	23.3	7×10^3 [e]
	[Si II] $^2P_{3/2} - ^2P_{1/2}$	34.8	9.4	8.1	3.4×10^5 [H], 1×10^3 [e]
	[Ar II] $^2P_{1/2} - ^2P_{3/2}$	7.0	2.0	15.8	4.0×10^5 [e]
MOPRA[c]	^{12}CO J = 1→0	2600	43	–	1.8×10^3 [H_2]
ASTE[d]	^{12}CO J = 3→2	867	22	–	3.2×10^4 [H_2]

Notes. [(a)] Critical densities are noted [e] for collisions with electrons ($T = 10\,000K$), [H] with hydrogen atoms ($T = 100\ K$) and [H_2] with molecular hydrogen ($T = 10\ K$, in the optically thin limit). [(b)] Indebetouw et al. (2009) [(c)] Wong et al. (2011) [(d)] Minamidani et al. (2011)

We process the FTS data using the *Herschel* Interactive Processing Environment (HIPE) version 11.0.2825 and the SPIRE calibration version 11.0 (Fulton et al. 2010; Swinyard et al. 2013). We use the method from Wu et al. (2013) to derive integrated intensity images and their uncertainties. This script has been recently used to generate FTS spectral cubes for M83 (Wu et al. 2015). A combination of parabola (continuum) and sinc (emission) functions is used to model a spectral line. The spectra are then projected onto a grid that covers a $5' \times 5'$ area with a pixel size of $15''$ (roughly corresponding to the detector spacing for SSW). We perform a Monte Carlo simulation with 300 iterations to estimate the uncertainties on the spectra, as described in details in Lee et al (in prep). The SNR is between 1 and 8 for [N II] 205 μm and between 0.5 and 5 for [C I] 370 μm. The [C I] 609 μm is weaker and the SNR is below 2.

The maps of [N II] 205 μm and [C I] 370 and 609 μm are presented in Figures 1 and 2. Properties of these lines are presented in table 1. CO transitions from J = 4 – 3 to J = 13 – 12 were also observed in 30Dor and will be presented in Lee et al. (in prep).

2.3. *Herschel* and *Spitzer* photometry

To constrain the PDR models, we need to calculate the infrared luminosity, which requires photometry data from mid-infrared (MIR) to sub-millimeter. PACS and SPIRE maps of the Large Magellanic Cloud at 100, 160 250, 350 and 500 μm were first published in Meixner et al. (2013) as part of the HERITAGE project. We also use the observations of 30Dor obtained as part of the *Spitzer* (Werner et al. 2004) Legacy program "Surveying the Agents of a Galaxy's Evolution" (SAGE ; Meixner et al. 2006). We used the four channels of IRAC (Fazio et al. 2004) at 3.6, 4.5, 5.8 and 8.0 μm and MIPS (Rieke et al. 2004) observations at 24 and 70 μm. The MIPS 24 μm map is saturated in several pixels. We use the IRS spectra (Indebetouw et al. 2009; see also Sect. 2.4) to calculate the 24 μm synthetic photometry in the MIPS 24 bandpass and compare to the original map, with excellent agreement in parts where the Spitzer/MIPS map is not saturated. Table 2 summarizes the photometry data we use to construct the infrared luminosity, associated with their spatial resolution.

Table 2. Properties of the photometry data.

Instrument	λ (μm)	FWHM (arsec)
IRAC[a]	3.6	1.7
	4.5	1.7
	5.8	1.7
	8.0	1.9
MIPS	24	6
	70	18
PACS[b]	100	7.7
	160	12
SPIRE[b]	250	18
	350	25
	500	37

Notes. [(a)] SAGE (Meixner et al. 2006) [(b)] HERITAGE (Meixner et al. 2013)

2.4. *Spitzer* / IRS spectroscopy

The Spitzer IRS low resolution data have been initially presented in Indebetouw et al. (2009). The observed lines and their spatial resolution are listed in Table 1. We have reduced again the low spectral resolution cubes with CUBISM (Smith et al. 2007a) as part of an effort to measure lines that have not been investigated yet in detail, in particular the H_2 lines, [Si II] and [Ar II]. The resolving power of both the short-wavelength/low-resolution (SL) and the long-wavelength/low-resolution (LL) modules range approximately from 60 to 120 (*Spitzer* Observer's Manual 7.1 2006[1]). The maps of [Si II], [S III] 18 μm and [S III] 33 μm are presented in Figure 1.

We use the total emission of the polycyclic aromatic hydrocarbon molecules (PAHs) that has been fitted by Indebetouw et al. (2009) using the package PAHFIT (Smith et al. 2007b). Finally, we also use the Spitzer IRS high-resolution spectra presented by Lebouteiller et al. (2008) to measure the H_2 lines.

[1] Available at http://ssc.spitzer.caltech.edu/documents/SOM.

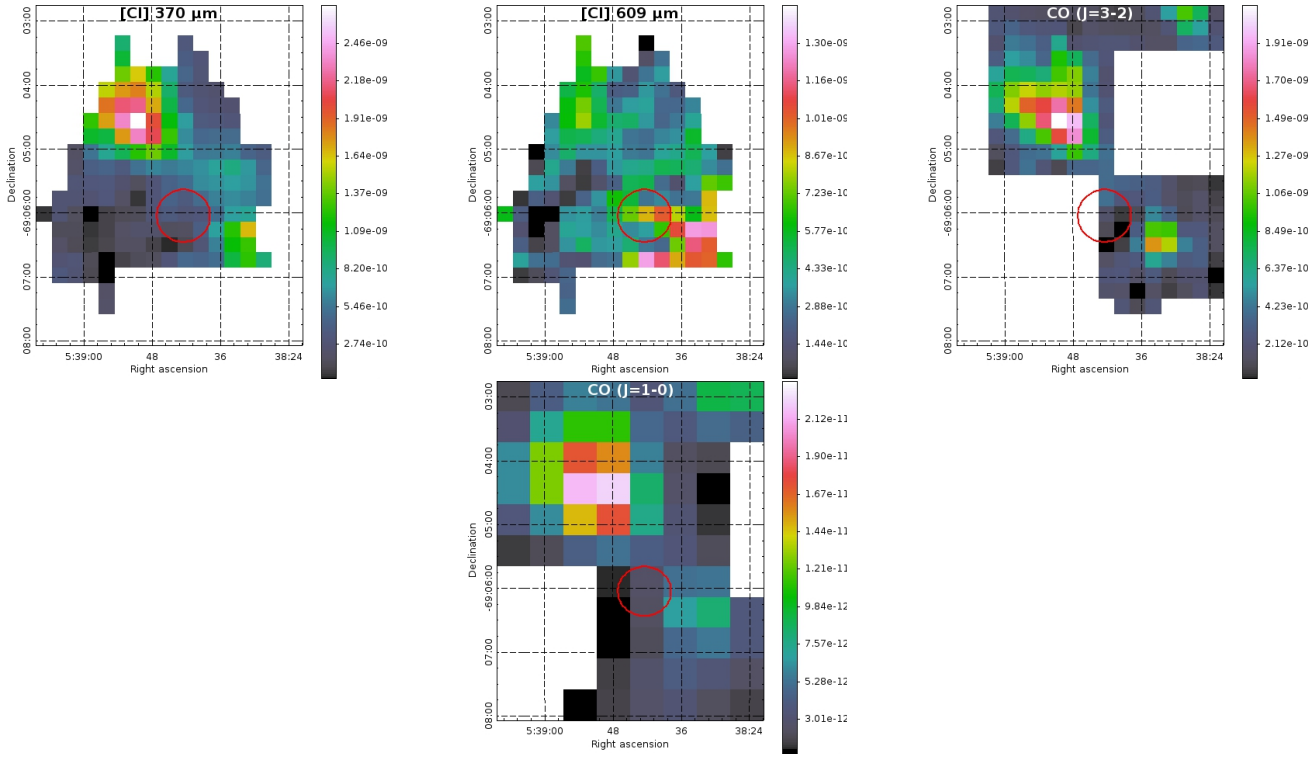

Fig. 2. *Top panel*: [C I] 370 μm (*left*) and [C I] 609 μm (*right*) SPIRE/FTS maps of 30Dor. *Bottom panel*: CO (3-2) ASTE map (*left*) and CO (1-0) MOPRA map (*right*). All of the maps are shown at their original resolution, in W m^{-2} sr^{-1}. The circle shows the location of R136. Table 1 and Section 2 describe these observations in detail.

2.5. Ground-based observations

Low-J CO transitions are required for additional constraints for the PDR modeling. We use the CO J = 1 – 0 transition observed with MOPRA (Wong et al. 2011) and CO J = 3 – 2 observed with ASTE (Minamidani et al. 2011, see Figure 2). The spatial resolutions for the MOPRA and ASTE data are 42″ and 22″ respectively.

The H_α emission, which we use as a qualitative tracer of the ionized gas, was observed with the Cerro Tololo Inter-American Observatory (CTIO) Curtis Schmidt telescope as part of the Magellanic Clouds Survey (MCELS, private communication; R.Leiton) at a resolution of $\sim$ 5″.

2.6. Convolution kernels

As we use line ratios of different wavelengths and different instruments (see Table 1), we must first convolve the maps to the same resolution. We add quadratically 12% uncertainties to the PACS maps to account for the absolute calibration uncertainties (PACS Observer's Manual v2.5.1). When we use only PACS observations, all of the maps are convolved to the resolution of PACS at 160 μm (12″ or $\sim$ 3 pc), using the kernels from Aniano et al. (2011).

When we combine PACS, SPIRE and ground based spectroscopy data together to include the [C I] and CO lines (see Sect. 4.4), all of the maps are smoothed to match the resolution of 42″ ($\sim$ 10 pc), limited by the SPIRE long wavelength data. For this, we use the appropriate kernels to convolve a PACS point spread function (modeled by Aniano et al. 2011) to the SPIRE/FTS beam profile (fitted by a two-dimensional Hermite-Gaussian function) at the lowest resolution, essentially following the method by Gordon et al. (2008).

The photometry bands are used to determine the infrared luminosity with our spectral energy distribution (SED) model (see Sect. 2.7). Since we wish to perform the PDR analysis on the smallest possible scale (i.e. limited by the PSF of the PACS [C II] map), we calculate the infrared luminosity at the resolution of 12″, which is also the resolution of the PACS 160 μm band. We have compared this approximated infrared luminosity to that determined using all available bands, i.e., including the SPIRE bands (250, 300 and 500 μm). We find little difference on the integrated luminosity per surface area. Thus we include only the bands between 24 and 160 μm to fit the SED at the best spatial resolution possible.

2.7. Infrared luminosity maps

For each pixel of the map, we construct the full MIR to submm SED, to which we apply the dust SED model of Galliano et al. (2011, AC composition). This is a phenomenological SED fitting procedure with which we derive the resolved total infrared luminosity (L_{TIR}) between 3 and 1000 μm, as well as the far-infrared luminosity (L_{FIR}) between 60 and 200 μm. This model was designed to fit the *Herschel* broadband photometry of the LMC, still remaining consistent with the elemental abundances. The free parameters include the dust mass (from which the extinction magnitude in V band, A_V^{dust}, can be derived), the minimum starlight intensity, the difference between the maximum and minimum starlight intensities, the starlight intensity distribution power-law index and the PAH-to-total dust mass ratio f_{PAH}. The final map of L_{TIR}, which integrates the SED fit between 3 and 1000 μm, can be seen in Figure 1. Contrary to other dust parameters, the infrared luminosity is very marginally model dependent. It depends mainly on the wavelength coverage of the photometric constraints used, which in our case is sufficient. For

the PDR modeling (see Section 4) we use the L_{FIR} integrated between 60 and 200 μm. The SED model is better constrained in this limited wavelength range compared to the fit including longer wavelengths so this leads to less uncertainties on L_{FIR}. However, even with no constraint longward 160 μm, the L_{TIR} of 30Dor is still relatively well constrained, as the dust in this region is sufficiently warm to peak at much shorter wavelengths.

3. Data analysis

3.1. General morphology

Figure 1 shows the maps of H_α, [O III], [S III], [N II], [C II], [Si II] and [O I] lines at their initial resolution. We also show the L_{TIR} (integrated between 3 and 1000 μm) as well as the PAH emission (L_{PAH}). The emission of all lines is distributed in the northern and southern lobes around R136. The emission of all lines peaks near the same location within 5 pc towards the northern lobe, with some inhomogeneous emission in the south. The spatial distributions of the [C I], CO(1-0) and CO(3-2) emission are presented in Figure 2. They show two lobes of emission as well, and the peaks of both the [C I] and CO emission are shifted about 20″ north of the peak of [C II].

The [C II], [O I] and L_{PAH} follow approximately each other throughout the map. The [O I] 63 μm, [O I] 145 μm and [C II] emission lines, as well as L_{PAH}, are PDR tracers, although there may be a diffuse component as well, which could be contributing to the emission of [C II] (see Section 3.2).

The distributions of the H_α, [O III] 88 μm, [S III] and [N II] lines have a structure different from the neutral PDR tracers [C II] and [O I]. The spatial distributions of [O III], [S III] and [N II] follow well the distribution of the ionized gas traced by H_α emission and show in particular a characteristic arm-like structure in the north-east of R136. The ionization potentials of O^{++} and S^{++} are respectively 35 eV and 23.3 eV (see table 1), so [O III] 88 μm and both [S III] 18 μm and [S III] 33 μm probe the highly ionized gas. The peak of [O III] is shifted from that of [C II] toward the south, in the direction of R136. The peak of [N II] 122 μm is located between the peaks of [O III] 88 μm and [O I], as expected from the values of the ionization potential of each specie. [N II] traces the low density and low-excitation ionized gas (critical density for collision with electrons are ~310 cm^{-3} and ~48 cm^{-3} for [N II] 122 μm and [N II] 205 μm respectively).

The distributions of [Si II] 35 μm and L_{TIR} emissions share properties both with the ionized gas ([O III] and [S III]) and the PDR tracers ([O I] and [C II]). The [Si II] 35 μm line and the L_{TIR} can in principle be used as a PDR tracer, but we also find in the maps some features that seem spatially associated with the ionized gas as well. This is discussed in Sections 3.2 and 3.4.

Figure 3 shows the different layers of the ISM, from the ionization front near the stellar cluster, where the highly ionized gas traced by the [S IV] 10.5 μm emission is located, to lower ionization states ([Ne II] 15.6 μm) and then to the PDRs traced by [C II]. The CO peak is located close to the [C II] peak. This spatial disposition suggests that R136 dominates the photoionization. We can also see that the northern region seems to be quite well shielded from ionizing UV photons, since [C II] is very extended in this direction while the tracers of the ionized gas show a sharp decrease on the other side of the H_α arc.

The [O III] 88 μm is the brightest FIR line in 30Dor, as in N11, the second largest H II region of the LMC (Lebouteiller et al. 2012), the dwarf galaxy Haro 11 (Cormier et al. 2012)

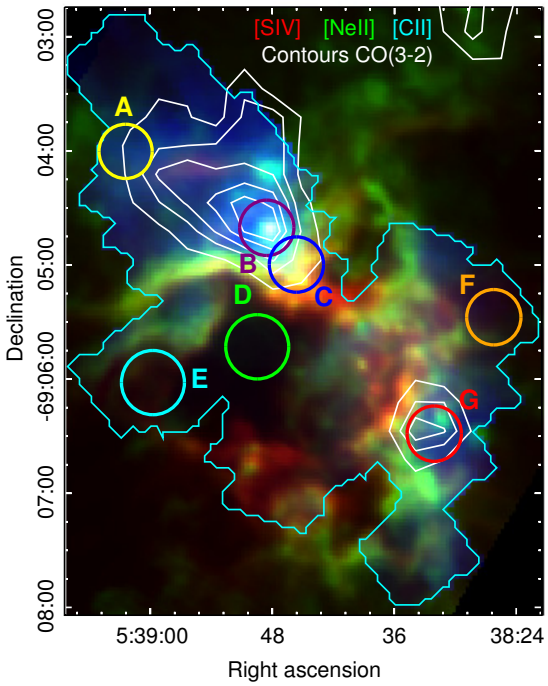

Fig. 3. Red: Spitzer/IRS [S IV] 10.5 μm (Indebetouw et al. 2009). Green: Spitzer/IRS [Ne II] 12.8 μm (Indebetouw et al. 2009). Blue: PACS [C II] 158 μm. The blue contours outline the limit of the [C II] map. We can identify the different layers of the gas from the highly ionized medium near the star cluster R136 to the clumpy molecular gas. In white are the contours of the ^{12}CO(3-2) emission observed with ASTE (Minamidani et al. 2011). The yellow region (A) is located on the north-east of R136, where [C II] is extended but where [O III] seems fainter. The violet circle (B) is located on the [C II] peak, the blue circle (C) on the [O III] peak. The green (D), cyan (E) and orange (F) circles probe more diffuse regions. The south-west peak of [C II] is in the red region (G).

and in most of the dwarf galaxies (Cormier et al. 2015), integrated over full galaxy scales. This was first noted in several dwarf irregular galaxies in Hunter et al. (2001). [O III] is brighter than [C II] by a factor of 2 to 60 throughout our 30Dor map. Figure 4 shows the ratio [O III]/L_{TIR} versus [C II]/L_{TIR} in 30Dor. Cormier et al. (2015) already noted the elevated [O III] 88 μm/L_{TIR} in dwarf galaxies compared to the normal galaxies of Brauher et al. (2008). Given that it requires 35 eV to ionize O^+ to O^{++}, this suggests the presence of high temperature stars throughout the region. The range of [C II]/L_{TIR} values covered in 30Dor is very broad (more than an order of magnitude) and they cover almost the entire range of [C II]/L_{TIR} observed in the wide range of galaxy type in Brauher et al. sample. The [O III]/L_{TIR} distribution is narrower (about a factor of 6 over the map). The regions with the highest L_{TIR} are the peaks of [O III] and [C II] (Fig. 3, regions C and B). The highest [C II]/L_{TIR} ratio is found in the northern part of 30Dor (near region A): this is due to the fact that L_{TIR} decreases more rapidly than [C II] with increasing distance from the exciting sources.

In the regions where [C II] is the brightest, the line intensities of [O I] 63 μm and [Si II] are similar to the [C II] intensity. [O I] 63 μm is everywhere at least ten times brighter than [O I] 145 μm. The map of [N II] 122 μm is the smallest and this line is also the faintest of our PACS lines (at least 200 times fainter than [O III]), but the SNR throughout the region mapped is ≥5. The [N II] 205 μm emission is 1 to 3 times fainter than [N II]

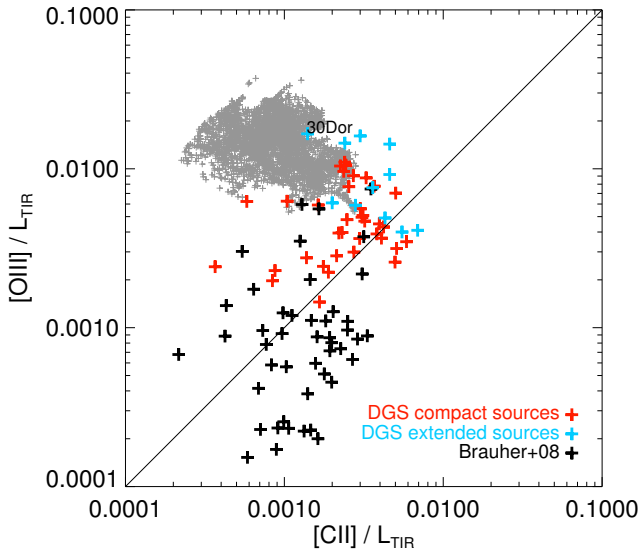

Fig. 4. [O III]/L_{TIR} versus [C II]/L_{TIR}. The regions in 30Dor form the grey cloud with the high [O III]/L_{TIR} values. The DGS galaxies (Cormier et al. 2015) are represented by red (compact) and cyan (extended) symbols. The (mostly) metal-rich galaxies from Brauher et al. (2008) are represented by black symbols.

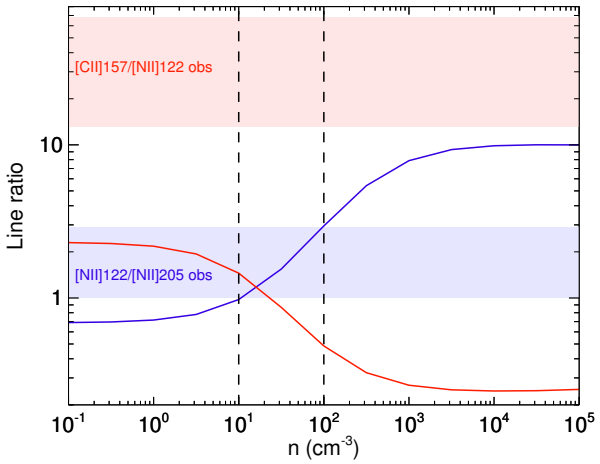

Fig. 5. Theoretical ratios [N II] 122 μm / [N II] 205 μm (blue) and [C II] / [N II] 122 μm (red) at the temperature of 10 000 K. Blue and red areas indicate our observed ranges for the [N II] 122 μm / [N II] 205 μm and the [C II] / [N II] 122 μm ratios respectively. The observed values of the [C II]/[N II] ratio (in red) are much higher than the theoretical value in the ionized gas for the entire map, indicating that [C II] is mostly emitted in the PDRs and not in the ionized gas.

122 μm.

3.2. Origin of [C II] and [Si II] emission

Because the ionization potential of C^0, 11.3 eV, is lower than 13.6 eV, the [C II] line can originate either from the PDRs or from the ionized gas. We thus need to investigate the possible contribution from the ionized gas and from PDRs to the [C II] emission before we can use it as a PDR tracer and a constraint for PDR modeling.

Following the analysis of Oberst et al. (2011), we use the fact that the ratio [C II]/[N II] 122 μm can be calculated theoretically in the ionized gas, and that [N II] originates only from the ionized gas. We calculate the fine-structure level populations of C^+ and N^+ as a function of the density using the theoretical collisional rates. We then apply a correction factor due to the ionic abundance fraction $\frac{C^+/C}{N^+/N}$. We used the MAPPINGS III photoionization grids (Allen et al. 2008) and found that this fraction depends little on the conditions (ionization parameter, starburst age, density) with a value around 0.85 ± 0.15. Finally, we scale the emission ratio with the observed elemental abundances of C and N in 30Dor from Pellegrini et al. (2011) listed in Table 3. The final ratio [C II]/[N II] 122 μm depends strongly on the electron density between 1 and 1000 cm^{-3}. Since the critical densities for [N II] 122 μm and [N II] 205 μm are 310 cm^{-3} and 50 cm^{-3} respectively (Table 1), the ratio [N II] 122 μm/[N II] 205 μm is a good density tracer for the relatively low density ionized gas phase. We calculate the ratio [N II] 122 μm/[N II] 205 μm to determine the density using the theoretical curve from Bernard-Salas et al. (2012) (see Figure 5). This ratio depends only slightly on the temperature ; we choose a typical temperature of 10 000K. The calculated density presented in Figure 6 ranges from 10 to 100 cm^{-3}. Our values fall in the low density regime of the [S III] line ratio, which is sensitive to high density (n_{crit} = 1.5×10^4 cm^{-3} for [S III] 18 μm and n_{crit} = 4.1×10^3 cm^{-3} for [S III] 33 μm), and does not provide a useful constraint.

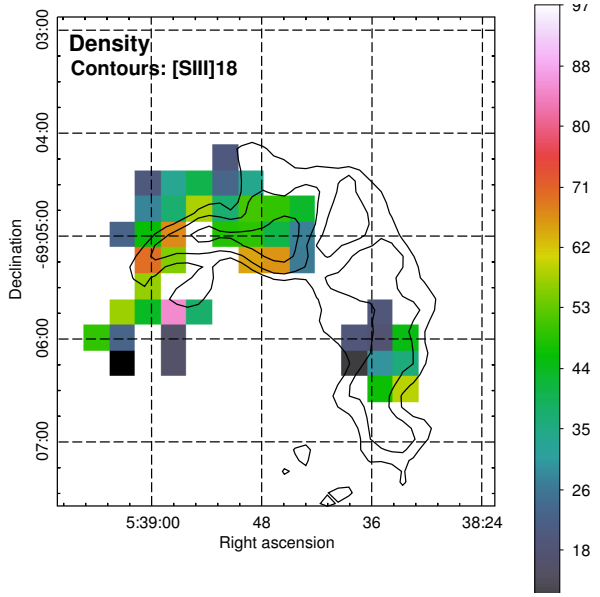

Fig. 6. Electron density in cm^{-3} calculated from the ratio [N II] 122 μm / [N II] 205 μm. The pixel size is 20″ (∼ 5pc). The black contours represent the emission of the ionized gas tracer [S III] 18 μm.

If the [C II] emission would originate in the low density ionized gas traced by [N II], the [C II]/[N II] 122 μm ratio would be ∼ 0.5 − 1.3 (Fig. 5). However, the observed ratio is significantly higher by a factor of ∼ 10 than this theoretical ratio in the ionized gas. At least 90% of the [C II] is expected to be emitted from PDRs in the entire mapped region. The [C II] emission can be considered to be a reliable tracer of the PDR gas in 30Dor.

Since the density is known and [Ar II] originates from the ionized gas, we can also calculate the theoretical ratio [C II]/[Ar II] in the ionized gas. Similarly, comparing the observed ratio [C II]/[Ar II] to the theoretical ratio in the ionized

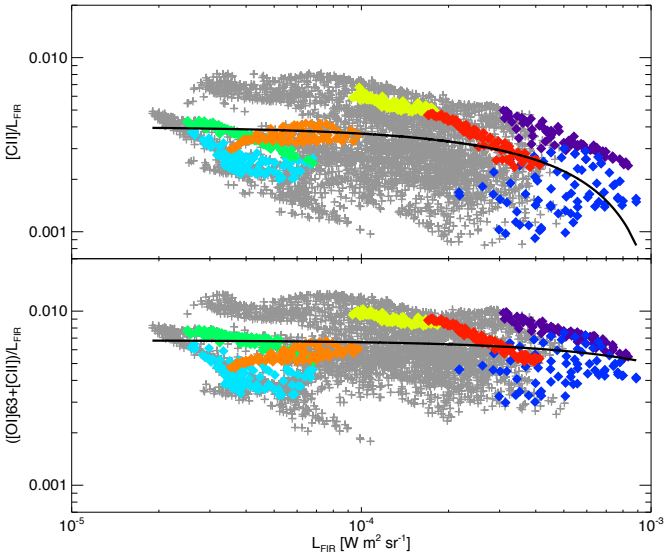

Fig. 7. *Top*: Ratio of [C II]/L_{FIR} versus L_{FIR}. The color symbols are associated with the regions defined in figure 3. The grey symbols are all of the other pixels of our 30Dor map. The black curve shows a linear regression of the data. *Bottom*: Ratio of ([O I] 63 μm+[C II])/L_{FIR} versus L_{FIR}.

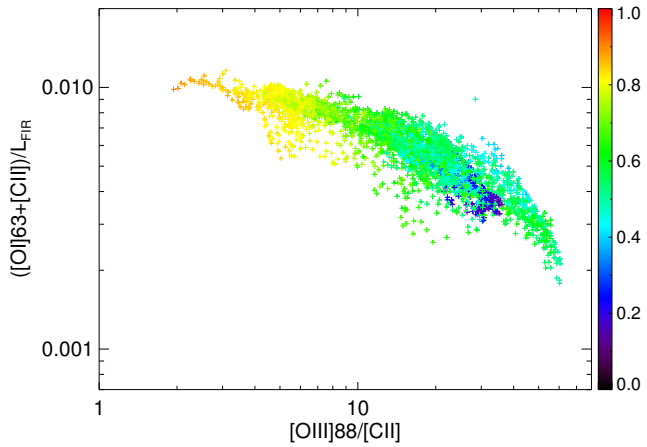

Fig. 8. Ratio of ([O I] 63 μm+[C II]) /L_{FIR} versus [O III]/[C II]. The color bar indicates the fraction of L_{FIR} expected to come from the PDRs (see Section 3.4).

gas, we also deduce that a large fraction (> 95%) of the [C II] emission originates from the PDRs.

[Si II] emission can also originate from PDR or ionized gas. We proceed with the same method to separate the emission of the ionized gas from that of the neutral gas. The critical density of [Si II] is close to that of [Ar II] (3.4×10^5 cm^{-3} and 4.0×10^5 cm^{-3} respectively, see Table 1) and both the observed ratios of [Si II]/[Ar II] and [Si II]/[N II] are consistent with 60% to 90% of the [Si II] emission originating from the PDRs.

3.3. The photoelectric heating efficiency

The top panel of Figure 7 shows the observed [C II]/L_{FIR} ratio as a function of L_{FIR} for every pixel of the PACS map. The ratio [C II]/L_{FIR} is often used to estimate the fraction of energy absorbed by dust that is used to heat the gas via the photoelectric effect (the photoelectric heating efficiency). This ratio ranges between 0.1% and 1% with a significant scatter – about one order of magnitude. We observe a tendency of decreasing [C II]/L_{FIR} as L_{FIR} increases (same trend as in Stacey et al. 2010), with a slope of -3.6 ± 0.2. However, when we add the [O I] 63 μm emission (lower panel of Figure 7), we find a smaller dispersion (with a factor of 7) and also a flatter relation between ([O I] 63 μm+[C II]) / L_{FIR} and L_{FIR}, with a slope of -1.4 ± 0.3 for the linear regression. Both [O I] and [C II] are contributing noticeably to the cooling of the gas, as shown in Lebouteiller et al. (2012).

Figure 8 shows that the decrease of the ratio ([O I] 63 μm+[C II])/L_{FIR} is mostly due to the ionized component part in L_{FIR}. Indeed, the ratio ([O I] 63 μm+[C II])/L_{FIR} is well correlated with the ratio [O III] 88 μm/[C II], and it decreases with increasing [O III] 88 μm/[C II], which is representative of the ionization state of the gas. If we subtract the IR contribution from the ionized gas (as described in Section 3.4), we find that the ratio ([O I] 63 μm+[C II])/L_{FIR} to be fairly constant and narrow.

3.4. The origin of the FIR emission

Although grains and PAHs in the PDRs contribute to the FIR emission, a fraction of L_{FIR} can also come from the H II regions, from big grains in equilibrium with the interstellar radiation field (ISRF). In this section, we inspect the origin of the L_{FIR} throughout the map, to separate the fraction in the ionized gas component from that in the PDR component. In order to separate the emission from these two components, we assume that the PAH emission traces the PDRs and [O III] traces the ionized phase. Indeed, we can see in Figure 1 that the spatial distribution of the L_{FIR} shows features similar to the PAH emission or any other neutral atomic gas tracer ([C II], [O I]), while other features seem to be spatially associated with [O III] or any other ionized gas tracers (H_α, [S III]). To disentangle the fraction of L_{FIR} in the ionized gas, we assume a linear relation such as: $L_{FIR} = \alpha \times L_{PAH} + \beta \times L_{[O\,III]}$. The pair of ($\alpha$; β) values is calculated using a multiple linear regression using all of the pixels in the map and is equal to (5.4 ; 11.5). This decomposition implicitly assumes that the PAH-to-dust mass fraction is constant in PDRs and zero in H II regions. The left panel of Figure 9 presents the correlation between [O III] 88 μm/L_{FIR} and L_{PAH}/L_{FIR}. The solid line on this plot shows the linear relation defined by: $\frac{L_{[O\,III]}}{L_{FIR}} = \frac{1}{\beta} - \frac{\alpha}{\beta} \times \frac{L_{PAH}}{L_{FIR}}$. With this method, we are seeking a first order correction of the total L_{FIR} to be able to use it for the PDR modeling. The modeled L_{FIR} reproduces the observed L_{FIR} within 30% on average. We determine the proportion of L_{FIR} coming from the PDRs as $L_{FIR}^{PDR} = \alpha\, L_{PAH}$. The result is presented on the right panel of Figure 9. On the north side of the map, far from the ionizing cluster, up to 90% of the FIR emission is expected to come from the PDRs, while on the east of the map, near the R136 cluster, about 70% of the FIR emission is expected to come from the ionized gas. We subtract the estimated fraction of L_{FIR} emitted in the ionized gas, using L_{FIR}^{PDR} for the PDR modeling.

3.5. Line ratios: empirical correlations

Far-infrared line ratios are useful diagnostics of the ISM conditions. We use these for PDR modeling (Section 4) and we inspect here their distribution throughout 30Dor. In Figures 10 and 11), we focus into different regions of 30Dor to inspect the

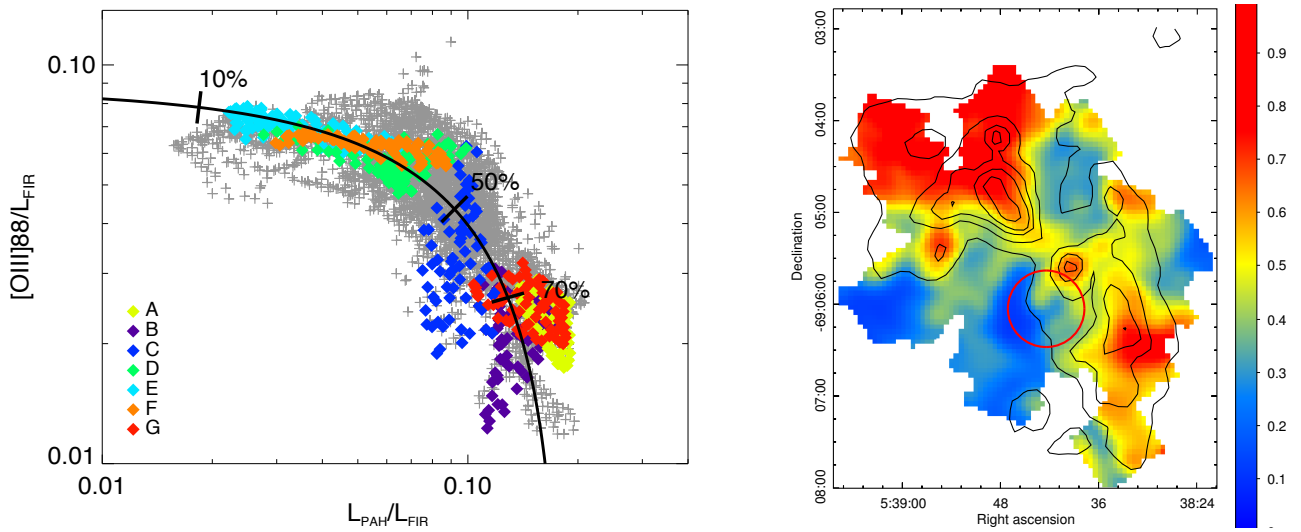

Fig. 9. *Left:* Ratio [O III] 88 μm/L_{FIR} as a function of L_{PAH}/L_{FIR}. The color symbols are associated with the regions defined in figure 3. The grey symbols are all of the other pixels of our 30Dor map. The solid curve shows the result of the multiple linear regression, using the values $\alpha = 5.4$ and $\beta = 11.5$. The values indicate the fraction of L_{FIR} coming from the PDR for 3 different positions on the curve. *Right:* Ratio of L_{FIR}^{PDR}/L_{FIR}. Black contours represent the total FIR emission. Close to the location of R136, only 20 to 30% of the L_{FIR} come from the PDRs.

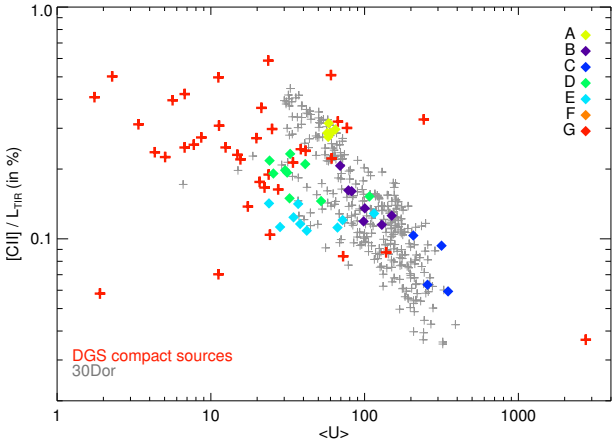

Fig. 10. Correlation between [C II]/L_{TIR} and <U> (average of the starlight intensity distribution). The red symbols are for the DGS galaxies (Cormier et al. 2015). The colored diamonds correspond to the regions of 30Dor illustrated in Figure 3

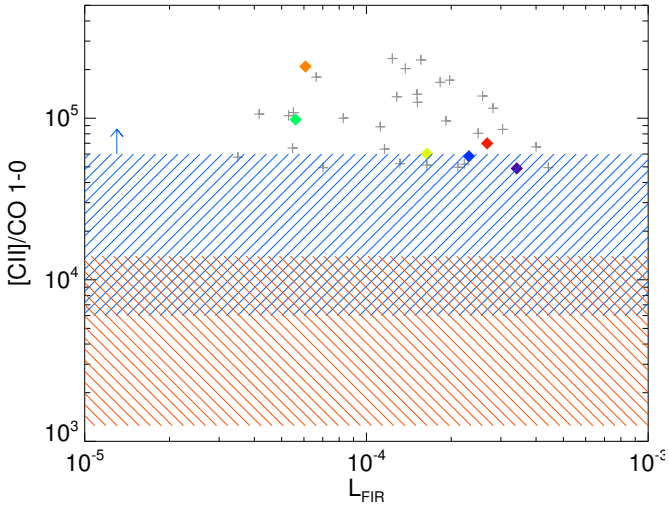

Fig. 11. Ratio of [C II]/ CO(1-0) versus L_{FIR} at the scale of 30″. The dashed horizontal orange band indicates the observed ratio [C II]/C0(1-0) in star-forming regions of the Galaxy and metal-rich galaxies (Stacey et al. 1991). The dashed horizontal blue band indicates the range of observed ratios for 6 bright sub-solar metallicity galaxies of the DGS (Cormier et al. 2014).

local variations.

To study how the distribution of starlight affects the observed photoelectric heating efficiency, we compare the average modeled starlight <U> from the SED modeling (see Sect. 3.4) with [C II]/L_{TIR} (Fig. 10). Note that we use the total L_{TIR} here since we do not know the fraction of the PDR component for the DGS sources. We compare our spatially resolved values with the distribution of <U> and [C II]/L_{TIR} from the integrated DGS compact sources of Cormier et al. (2015) and Rémy-Ruyer et al. (2014). More details and references can be found in Cormier et al. (2015). We see that 30Dor covers a large range in [C II]/L_{TIR}, approximately one order of magnitude, and approximately one order of magnitude in <U>.

There is a trend of decreasing [C II]/L_{TIR} as <U> is increasing, following the trend observed by Cormier et al. (2015), showing an apparent line deficit at high <U> values. This is probably an effect of the contribution of the ionized component to the infrared luminosity, as shown in Figure 8. The [O III] peak (region C in Figure 3) is the region with the highest <U>: it is the closest region to R136 in physical distance (see 5.3) ; the gas is mostly ionized. This region corresponds also to the lowest [C II]/L_{TIR} ratio.

To compare one of the primary PDR coolants with the CO(1 – 0), we show in Figure 11 [C II]/CO versus L_{FIR} at the resolution of 42″. [C II]/CO(1–0) throughout 30Dor is $\sim 5 \times 10^4 - 3 \times 10^5$. The observed range of the ratio [C II]/CO(1-0) is very broad. These values are about a factor 10 higher than the typical values for spiral or starburst galaxies ($\sim$ 2000 – 8000; Stacey et al. 1991; Negishi et al. 2001), and more in agreement with the range of values measured for integrated dwarf galaxies as already noticed in Poglitsch et al. (1995), Madden et al. (1997)

and Cormier et al. (2010, 2014). We note that low metallicity galaxies always show extreme [C II]/CO compared to the more metal-rich galaxies.

4. PDR modeling

In this section, we model the infrared observations of 30Dor using the Meudon PDR code and present results describing the properties of the gas.

4.1. The Meudon PDR model

The Meudon PDR code[2] is described in Le Petit et al. (2006), Le Bourlot et al. (2012) and Bron et al. (2014). It computes the atomic and molecular structure of interstellar clouds. The model considers a 1D stationary plane parallel slab of gas and dust illuminated by a radiation field (from UV to radio) arising from one or both sides. The radiative transfer is solved in an iterative way at each point of the cloud by taking into account absorption by gas and dust and scattering and emission by dust. For the present work, we used a development version (v1.6.0) with updates that includes the computation of X-ray radiative transfer and the impact on the chemistry and thermal balance of the cloud (Godard et al. in prep).

4.2. Input and output parameters

We describe here some of the configuration parameters of the model. We assume that the gas in each pixel can be modeled by a single cloud of pressure P, illuminated by a radiation field. The standard radiation field used in the Meudon PDR code is that observed in the solar neighborhood (Mathis et al. 1983) and is scaled with the parameter G_{UV} to control the intensity of the incident radiation field on each side of the cloud. For G_{UV} = 1, the integrated energy density between 911.8 Å to 2400 Å is 6.8×10^{-14} erg cm^{-3}. In the model we ran, G_{UV} ranges between 1 and 10^5 on one side and is fixed to 1 on the other side to expose this side to the general interstellar field. The pressure ranges between 10^4 and 10^8 cm^{-3} K. The pressure is constant throughout the cloud, however a constant density model has also been explored (Sect. 4.5). We have investigated the possibility of adding X-rays in the model, but found that they are not needed to explain the PACS observed data (Sect. 5.5). The visual extinction of the entire cloud has been varied from A_V^{max} = 1 magnitude to A_V^{max} = 10 magnitude. We estimate the mass fraction of PAHs from our SED modeling (Sect. 2.7). We find that f_{PAH} = 1% is adapted for 30Dor. We use elemental abundances as in Pellegrini et al. (2011) for He, C, N, O, Ne, Si and S, to reproduce as accurately as possible the conditions in 30Dor (see table 3). The dust-to-gas mass ratio is fixed to 0.5×10^{-3} based on our SED modeling (Sect. 2.7).

The output quantities computed by the model include the integrated line intensities and L_{FIR}, the ionic and molecular abundances, the emissivities and the chemical and thermal structure of the cloud. An example of the variations of the local gas phase abundances for some elements as a function of the depth into the cloud is presented in Figure 12 for a typical cloud of A_V^{max} of 10, with a constant pressure of P = 10^6 cm^{-3} K, illuminated by a radiation field of G_{UV} = 3000.

We use [O I], [C II] and L_{FIR}^{PDR} to constrain P and G_{UV} in the PDR model pixel by pixel. We consider here the observed [C II] emission without correction since the contribution from the ionized gas is low (Sect. 3.2) and we correct the L_{FIR} emission to remove the contamination from the component associated with the ionized gas (see Sections 3.2 and 3.4). At first we let A_V^{max} vary freely as this set of tracers cannot constrain this parameter and it has no influence on the resulting best model. This is illustrated in Figure 13, where we show the ratios $\mathcal{R}$ between several modeled line ratios and their observations for simulated clouds of different total depths. The ratios [O I]/[C II], ([O I]+[C II])/L_{FIR} are not very sensitive to A_V^{max}, as is also the case for the ratio [C I] 609 μm/[C I] 370 μm.

[2] The Meudon PDR code is public and available online at the following address: http://ism.obspm.fr.

Table 3. Input parameters for the PDR model.

Parameter	Notation	Value
Pressure	P	$10^4 - 10^8$ cm^{-3} K
Radiation field	G_{UV}	$1 - 10^5$
Cosmic ray flux	ζ^a	3×10^{-16} s^{-1}
Total visual extinction	A_V^{max}	1 – 10 mag
Metallicity	Z^b	0.5 $Z_\odot$
PAH fraction	f_{PAH}	1 %
Dust-to-gas mass ratio	M_{dust}/M_{gas}	5×10^{-3}
Gas phase abundances[c]		$log(n(X)/n(H))$
He		-1.05
C		-4.3
N		-4.91
O		-3.75
Ne		-4.36
Si		-5.51
S		-5.32

Notes. [(a)] Indriolo & McCall (2012); Indriolo et al. (2015) [(b)] Metallicity: 12+log(O/H) = 8.38 (Rolleston et al. 2002; Pagel 2003) and $(O/H)_\odot = 4.9\times10^{-4}$ (Asplund et al. 2009). [(c)] Pellegrini et al. (2011)

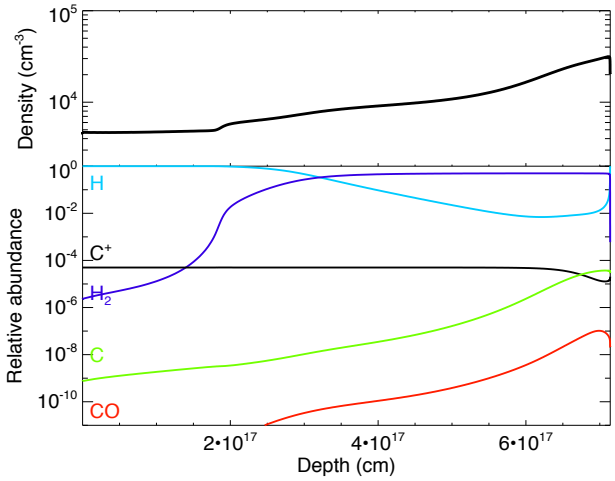

Fig. 12. *Top:* Density profile as a function of the depth into the cloud in a simulated cloud of A_V^{max}= 2, P = 10^6 cm^{-3} K with G_{UV} = 3000 on the left side and G_{UV}= 1 on the right side. *Bottom:* Local gas phase relative abundances of C$^+$, C, CO, O and H_2 for the same model.

4.3. Pressure and incident radiation field

We find the best solution for the incident radiation field and the pressure using the observed line intensities as constraints. They

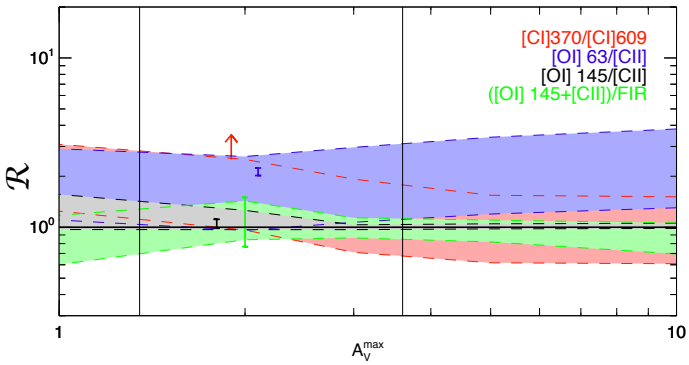

Fig. 13. Ratios, $\mathcal{R}$, of the modeled line ratios over the observed line ratios for [C I] 370 μm/[C I] 609 μm, [O I] 63 μm/[C II], [O I] 145 μm/[C II] and ([O I] 145 μm+[C II])/L_{FIR}^{PDR}, for simulated clouds of different A_V^{max} from 1 to 10, for 30Dor abundances. The width of the bands represents the dispersion of $\mathcal{R}$ throughout the map. The error bars due to uncertainties on the observations are plotted. The vertical lines indicate the range of A_V^{max} where the predictions of the model are compatible with the observed [C II]/ CO(3-2) (see Fig. 17).

are found by minimizing the χ^2 distribution :

$$\chi^2 = \sum_{j=1}^{N} \left(\frac{I_j(x,y) - M_j}{\sigma_j(x,y)} \right)^2, \quad (1)$$

where $I_j(x,y)$ is the observed value of the ratio i, for a given pixel (x,y), $\sigma_j(x,y)$ is the uncertainty associated with this observed ratio and M_j is the value predicted by the model for the ratio j. N is the number of constraints (independent ratios) that are used. Ratios of line intensities are used instead of absolute values. In this case, if species are co-spatial in the cloud and if there are no opacity effects, we can then ignore the effect of an area filling factor different than one and the presence of several clouds along the line of sight (see Sect. 5.1).

As an example, we present in Figure 14 the values of G_{UV} and P that reproduce the observed values for the ratios ([O I] 145 μm+[C II])/L_{FIR}^{PDR} in blue, [O I] 145 μm/[C II] in red and [O I] 63 μm/[C II] in cyan for two pixels of the map of 30Dor at 12″ resolution, located in the regions D and C (Fig. 3). We can see in these figures that the constraint given by the ratio [O I] 63 μm/[C II] is never consistent with the other ratios within the error bars. This is likely due to optical depth effects in the [O I] 63 μm line, as we show later in this section. For now, we will not consider this line to constrain the parameters of the model.

First, we use the ratios ([O I] 145 μm+[C II])/L_{FIR}^{PDR} and [O I] 145 μm/[C II] to constrain G_{UV} and P. Thus we are limited by the PACS resolution of 12″ and by the spatial coverage of the [O I] 145 μm map. We do not use the ratio [C I] 370 μm/[C I] 609 μm, which does not bring strong constraints on G_{UV} and P as the error bars are very large. We have then the same number of constraints and parameters. We can note from Figure 14 that there is a degeneracy between a high G_{UV}/low P solution and a low G_{UV}/high P solution. The addition of the ratio [C II]/[C I] or [C II]/CO does not help to break this degeneracy since they are very dependent on A_V^{max} (Sect. 4.4). However, the high G_{UV}/low P solution, highlighted with a green cross in Figure 14, has a lower χ^2 and is preferred based on the following arguments. Indeed, the high P solution requires high optical depths in [O I] 63 μm ([O I] 63 μm is over-predicted by a factor of up to 9, see below), while the A_V^{max} (determined as in Section 4.4) would be very low (< 1 mag). In addition, in the ionized gas we found a pressure P = $10^5 - 10^6$ cm^{-3} K for a typical temperature of 10 000K (see Section 3.2). We find a similar pressure in the PDR, suggesting that the gas may well be in pressure equilibrium. However, it must also be noted that Pellegrini et al. (2011) find a pressure somewhat larger using optical lines. Finally, a low G_{UV} solution results in large physical distances between the clouds and R136 (see Section 5.3), significantly larger (by a factor of ∼ 10 to 100) than found in Pellegrini et al. (2011).

We find G_{UV} ranging between 10^2 and 3×10^4 throughout the region and P between 10^5 cm^{-3} K and 1.7×10^6 cm^{-3} K, with $\chi^2 \sim 10^{-1}$ to 10^{-2} over the map[3]. The best P and G_{UV} maps are represented in Figure 15. The peaks of G_{UV} and P are almost co-spatial. The maximum is located north of R136, at the southern edge of the [O III] peak. It shows that there is a void around R136 and that the radiation field is first interacting with any matter a few parsecs away from the cluster. Details regarding the structure around R136 will be discussed in Section 5.3. The uncertainties associated with the observations, including calibration errors, lead to uncertainties on G_{UV} of +55%/-40% and on P of +/-12%.

The value of the observed ratio [O I] 63 μm/[C II] is lower than the ratio predicted by the model based on [C II], [O I] 145 μm and L_{FIR}^{PDR} by a factor of 1.3-2.5. This discrepancy between the predicted and the observed values may be due to optical depth effects of the [O I] 63 μm line (Tielens & Hollenbach 1985; Abel et al. 2007) or to absorption by cold gas along the line of sight (Liseau et al. 2006). As we can see from Figure 16 on the left, the lowest values of the ratio $\frac{([O\,I]\ 63\,\mu m/[C\,II])_{observed}}{([O\,I]\ 63\,\mu m/[C\,II])_{predicted}}$ correspond to the locations of the highest pressure. Since the difference between the observations and the model prediction seems to correlate spatially with the pressure here, it is probably not due to foreground absorption, but most likely from local effects. We can also note that the observed ratio [O I] 145 μm/[O I] 63 μm is larger than 0.1 in many pixels, which is an indication of optical depth effects in [O I] 63 μm (Tielens & Hollenbach 1985). In the best-solution model, the predicted ratio [O I] 145 μm/[O I] 63 μm is 0.04. The model accounts for the opacity of the lines for one cloud, but not between several clouds along the line of sight. If we examine one of the best solutions for region B ([C II] peak in Figure 3), the model predicts an opacity of 0.6 for [O I] 63 μm at $A_V = 1$ while that of [C II] is still below 0.1. Thus, if we have several components along the line of sight, the [C II] intensity can be multiplied by the number of components, while the [O I] 63 μm intensity increases less than linearly.

4.4. Determination of A_V^{max} using [C II], [C I] and CO

In this section we investigate the influence of A_V^{max} (that is, the total depth of the cloud, in magnitude) on the line ratios predicted by the Meudon PDR code. In Figure 17, we show the ratios $\mathcal{R}$ between several modeled line ratios and their observations for simulated clouds of different total depths. While the ratios [O I]/[C II], ([O I]+[C II])/L_{FIR} and [C I] 609 μm/[C I] 370 μm are not very sensitive to A_V^{max} (Fig. 13) , the ratios [C II]/[C I] and [C II]/CO vary by several orders of magnitude with the total depth of the simulated cloud, because they involve tracers that originate from different depths into the cloud. The observed ratios [C II]/[C I], [C II]/CO(1-0) and [C II]/CO(3-2) can be reproduced with a cloud of $A_V^{max} \sim 1 - 3$ mag per pixel of 30″ (7.2 pc)

[3] Note that this is not a reduced χ^2 as we have as many constraints as free parameters.

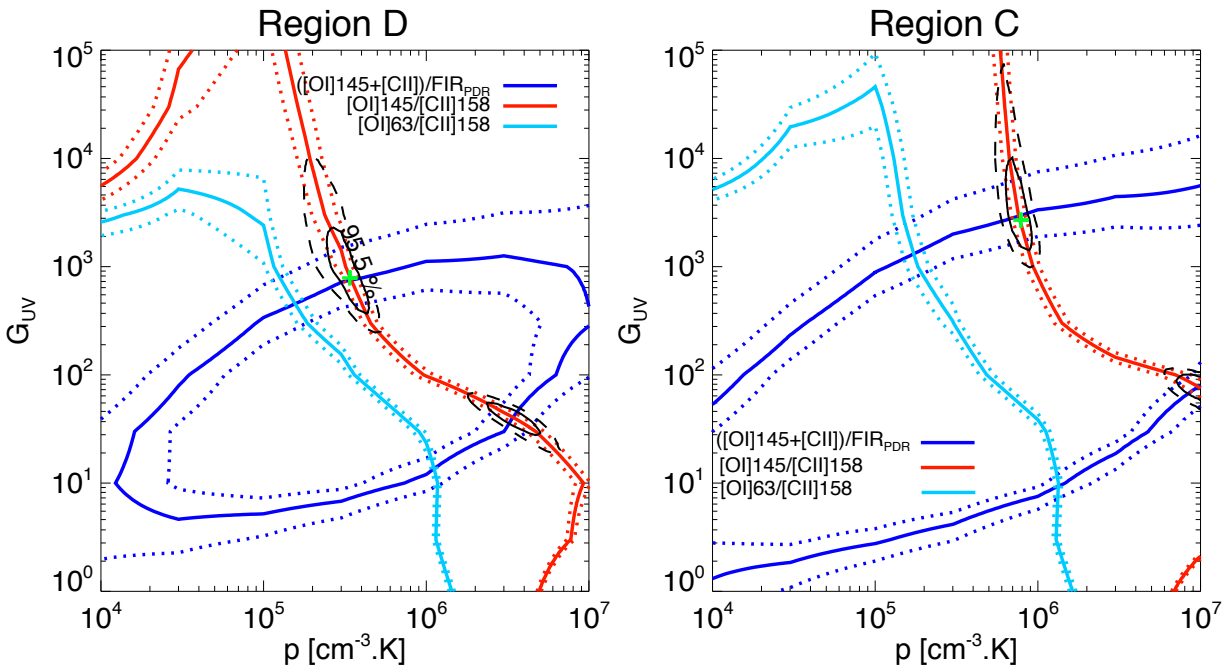

Fig. 14. Contour plots showing the parameters G_{UV} and P from our model, which reproduces the observed values of the ratios ([O I] 145 μm+[C II])/L_{FIR}^{PDR} (dark blue), [O I] 145 μm/[C II] (red) and [O I] 63 μm/[C II] (cyan). The dotted lines show the 1σ error on the observed ratios. The solid and dashed black contours represent the confidence intervals for, respectively, 1 and 2 σ. The green crosses indicate the best solutions for G_{UV} and P in each case, using ([O I] 145 μm+[C II])/L_{FIR}^{PDR} and [O I] 145 μm/[C II] as model constraints. Left plot is for a pixel representative of the region D (from Figure 3). Right plot is for a pixel from region C (from Figure 3), near the G_{UV} peak.

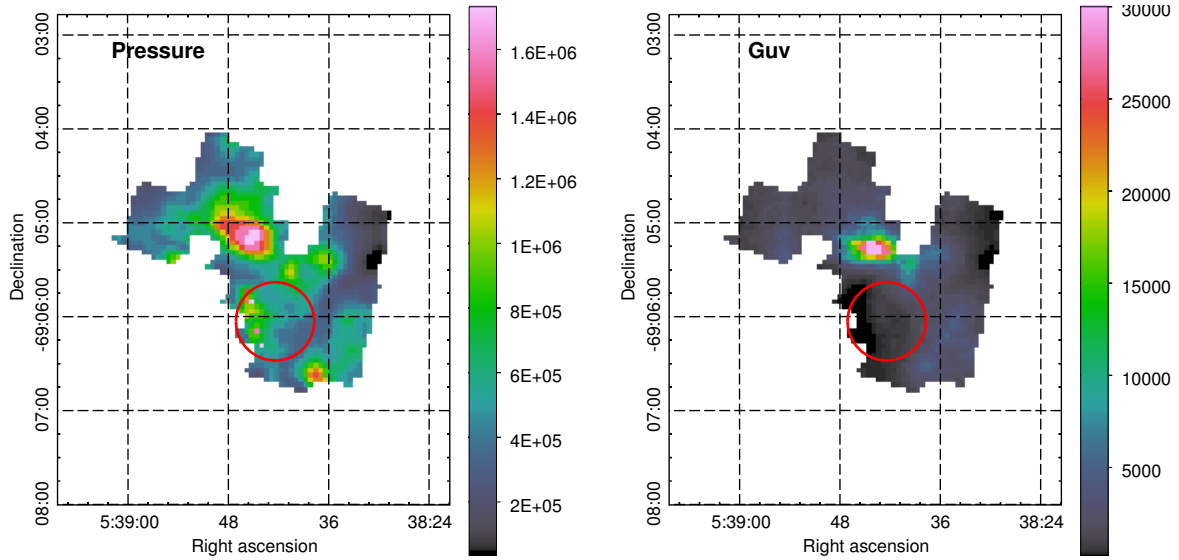

Fig. 15. Left: Best pressure map (cm^{-3} K) of the 30Dor region ; using ([O I] 145 μm+[C II])/L_{FIR}^{PDR} and [O I] 145 μm/[C II]. The total extinction for this model is A_V^{max}= 3. Right: Best G_{UV} map (color bar in units of the Mathis field) for the same model. The red circle shows the location of R136.

as shown in Figure 17, with G_{UV} and P determined as described in Section 4.3. However we keep in mind that the determination of this parameter is strongly dependent on the geometry of the model. This will be discussed in more details in Section 5.2.

4.5. Isobaric versus isochoric case

We considered a constant density model to compare our results with our isobaric model and with previous PDR model results. We use the same set of line ratios and the same χ^2 method to find the best radiation field and density predicted by an isochoric model.

We find a similar map for G_{UV} compared to our isobaric model, with a maximum of 20% difference between both cases. For the isochoric model, the density ranges between 3×10^2 to 1.4×10^4 cm^{-3}, with a spatial distribution quite similar to P in the isobaric case. This range of values is similar to those found by previous studies (e.g. Poglitsch et al. 1995; Bolatto et al. 1999; Röllig et al. 2006; Pineda et al. 2012). From the results of the isobaric model, we determine the density at the surface of the PDR. This initial density is about 1/2 to 2/3 the density determined with the isochoric model. In conclusion, the results from these two models are similar when applied to PDR line ratios.

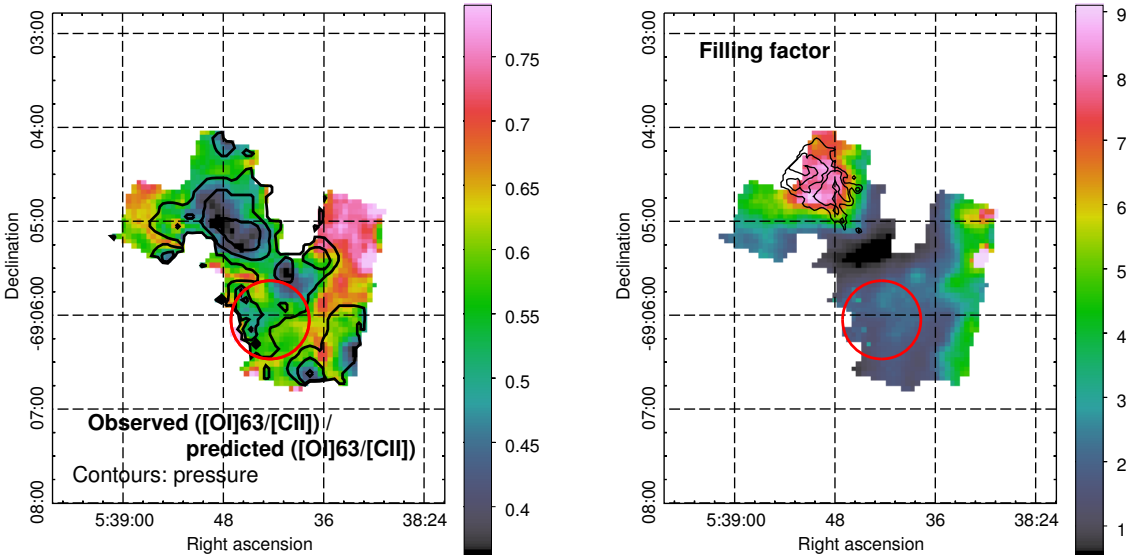

Fig. 16. Left: Ratio of the observed [O I] 63 μm/[C II] ratio over the predicted [O I] 63 μm/[C II] ratio (color bar). In black are the pressure contours, between 4.5×10^5 and 1.3×10^6 cm^{-3} K. The red circle shows the location of R136. Right: Filling factor Φ_A between 0.6 and 9 (color bar). The lowest values are at the peak of G_{UV}. The black contours represent the ^{12}CO(2-1) emission from ALMA (Indebetouw et al. 2013)

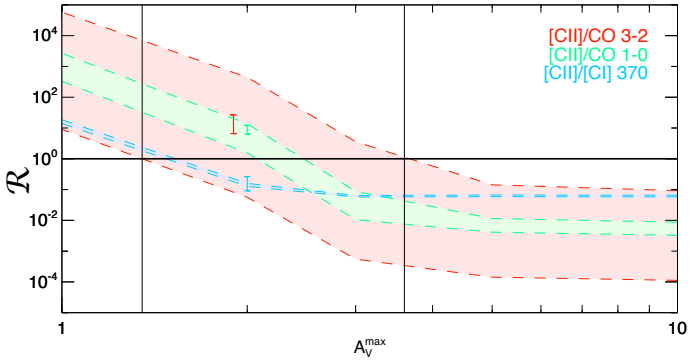

Fig. 17. Same as Figure 13, for the ratios [C II]/CO(3-2), [C II]/CO(1-0) and [C II]/[C I] 370 μm.

However, the predictions of the models start to diverge deeper into the cloud, in particular for molecular lines. Indeed, for an isobaric cloud of A_V^{max} of 3, the density rises by about a factor of 10, as the temperature drops, between the surface of the PDR and the core of the cloud (Fig. 12). This implies that the CO lines are emitted at lower A_V in a isobaric model compared to an isochoric model. As a consequence, the A_V^{max} probed by the observed CO lines is lower for an isobaric model than for an isochoric model. For example, the A_V^{max} probed with the low-J CO transitions (J=3–2 and J=1–0) is slightly higher for the isochoric model ($\sim 2-4$ mag) than the $1-3$ mag we find with the isobaric model. In conclusion, choosing the isobaric case is important to reproduce the higher J transitions of CO and quantify the CO-dark gas (see paper II), but it has little consequences for the results derived in this paper.

4.6. Model predictions for H_2 lines

H_2 is barely detected in the *Spitzer*/IRS low-resolution observations of 30Dor (Indebetouw et al. 2009). The model-predicted H_2 (0,0) $S(2)$ emission at 12.3 μm is 10 to 50 times lower than the upper limit from the observations. However, the emission from the high-resolution spectrum (Sect. 2.4) is in better agreement (by a factor of 2 to 5) with the model prediction.

Pak et al. (1998) measure H_2 (1, 0) $S(1)$ and (2, 1) $S(1)$ close to the CO (1-0) peak of 30Dor, with a beam of 81″. We compare these observations to the predictions of our model at 81″ resolution. Our map does not fully cover the 81″ beam. However, we calculate lower limits of 6×10^{-6} and 3×10^{-6} erg s^{-1}cm^{-2}sr^{-1} on the H_2 (1, 0) $S(1)$ and (2, 1) $S(1)$ emission respectively. There is a good agreement with the values measured by Pak et al. (1998) (10.8×10^{-6} and 4.0×10^{-6} erg s^{-1}cm^{-2}sr^{-1} respectively) considering we are missing some fraction of their beam. Rubio et al. (1998) present H_2 (1, 0) $S(1)$ observations at 1.16″ resolution. Their peak value of $4-6.10^{-5}$ erg s^{-1}cm^{-2}sr^{-1} is also consistent with our model results.

Yeh et al. (2015) have presented an H_2 (1, 0) $S(1)$ map of the entire 30Dor nebula at 1″ resolution. The peak H_2 surface brightness in their region A is 9.15×10^{-5} erg s^{-1}cm^{-2}sr^{-1}. Our model predicts a maximum H_2 surface brightness of 5.3×10^{-5} erg s^{-1}cm^{-2}sr^{-1} located near the [C II] peak, for a 12″ resolution. This is about a factor of 2 lower than the observed value, but it may be explained by the lower resolution used in our study and the fact that the H_2 emission could originate from clouds smaller than the PACS beam size.

5. Discussion

5.1. Filling factor

The model assumes that the PDR filling factor is unity, i.e., that the surface area of PDRs is equal to the beam area. If only part of the beam is covered or, on the contrary, if several clouds are present along the line of sight, the radiation emitted in the L_{FIR} and in cooling lines will be different than the model prediction for optically thin lines. The filling factor will be, respectively, lower or higher than 1.

G_{UV} and P have been determined only using ratios of lines coming from the same phase of the ISM. Thus, they do not depend on the filling factor because each line is affected by the same factor. The area filling factor, Φ_A, can then be estimated from the ratio of the observed intensity over the predicted intensity (for which $\Phi_A = 1$) for an individual line.

L_{FIR}^{PDR} and [C II] are both emitted by PDRs and scale with the filling factor in the same way. Thus, we can determine Φ_A either with $\frac{[C\,II]_{observed}}{[C\,II]_{predicted}}$ (as in Wolfire et al. 1990) or similarly with $\frac{L_{FIR\ observed}^{PDR}}{L_{FIR\ predicted}^{PDR}}$. This result is presented on the right panel of Figure 16. Φ_A is the smallest (about 0.6) near the peak of G_{UV}, in region C (Fig. 3). The maximum value is ∼ 9 on the north-east of the cluster. As stated earlier, an area filling factor greater than one means that several clouds covering the entire pixel are along the line of sight. Note that this approach is marginally coherent near the peak of [C II] where the maximum filling factor is ∼ 9. As noted in Section 4.3, considering that the opacity of [C II] is close to 0.1 at the [C II] peak, 9 clouds on the line of sight will add up to an opacity close to 1. As a consequence, the [C II] intensity will not add up linearly and this may call into question our assumption of optically thin [C II] at the [C II] peak location. Different PDR viewing angles can also affect this scenario and the number of components we derive is an upper limit.

This spatial distribution of the filling factor reflects the idea that the PDR clouds are smaller and/or less numerous where the radiation field is higher. The region mapped with ALMA by Indebetouw et al. (2013) corresponds to the region where the filling factor of PDRs is the largest in the map (see Figure 16). The CO emission is highly structured, showing dense (10^3–10^5 cm^{-3}) clumps and filaments, on sub-parsecs scales, covering approximately 10% of the area of the map. They observed significant photodissociation of CO by radiation penetrating between the dense clumps, which can explain the increased X_{CO} factor determined for unresolved low metallicity clouds. Indebetouw et al. measure an X_{CO} factor two times the solar-metallicity value in the dense CO clumps. This value can be even higher when possible interclump H_2 is included, for unresolved studies.

5.2. Clouds geometry

Indebetouw et al. (2013) observed the giant molecular cloud 30Dor-10, north of R136 with ALMA during Cycle 0 (it includes our regions B and C from Figure 3). In the region mapped with ALMA, they measure a maximum diameter of 1.2 pc for the CO(2-1) clumps and a filling factor of about 10%. This could mean that the CO luminosity is dominated by small, bright clouds in the CO beam and the medium could be characterized by clumps/filaments of low volume filling factor, with a physical size much smaller than our pixel size, implying that a plane parallel geometry together with the high filling factor determined with [C II] may not be adapted to our observations.

Indeed, with the A_V^{max}, G_{UV} and P previously determined in Sections 4.4 and 4.3, we find that several plane parallel clouds are required to reproduce the observed absolute intensities. Each of these clouds have a physical size between 0.2 and 3 pc, and an internal CO layer (estimated where the CO abundance is at least 50% of the maximum CO abundance) that ranges between 0.06 to 0.5 pc. The derived size scale is compatible with the ALMA observations. These results however depend on two main assumptions: the plane parallel geometry and the uniformity of PDR clouds in each pixel.

With a plane geometry, the A_V^{max} of the simulated clouds determined here by comparison of the [C II] and CO emissions can be considered as a lower limit. Indeed, adopting a different geometry by post-processing the results of the model and wrapping the plane-parallel results on a spherical geometry will result in a larger A_V^{max}. More details about this method can be found in Appendix B. When assuming a spherical geometry, bathed in an isotropic radiation field, a higher A_V (∼ 20 mag at the center of the cloud) is needed to reproduce the CO observations. Such extinction corresponds to spherical clouds with diameters about four times larger than the size of the optimal plane parallel clouds. Nevertheless the results derived in Section 4.3 for G_{UV} and P are independent on the assumed geometry and remain unchanged.

We note that the extinction parameter can be determined independently from the dust mass surface density, at a resolution of 22" (Sect. 2.7). We can then compare A_V^{dust} derived from the dust map to A_V^{max} derived using the [C II]/[C I] and [C II]/CO ratios in our PDR models (Sect. 4.4). On the one hand, A_V^{dust} corresponds to the integrated extinction along the line of sight in each pixel. On the other hand A_V^{max} is calculated for individual clouds, so for a meaningful comparison we need to scale by the number of components (i.e., the filling factor Φ_A; Sect. 5.1). While Φ_A is calculated at a relatively high spatial resolution (12″), the A_V^{max} for individual clouds is not well constrained due to the poor spatial resolution (42″) and coverage of the [C I] and CO maps. In Figure 18, we plot A_V^{dust} as a function of Φ_A (recalculated at a resolution of 22″), with several tracks showing the scaling with different A_V^{max} values. There is a remarkable correlation between A_V^{dust} and Φ_A, with most data points lying between the A_V^{max} = 1 and 3 lines, in agreement with the values determined with a plane-parallel geometry (Sect. 4.4). We emphasize that the determinations of A_V^{max} and Φ_A are quite independent from the determination of A_V^{dust}, as the two quantities are derived from different physical processes, and constrained by different observational sets. From Figure 18, we infer that most clouds share similar A_V^{max} values at a spatial resolution of 22″. Moreover, the good agreement between A_V^{dust} (total extinction) and A_V^{max} (derived in the neutral gas of PDRs) suggests that (1) there is no significant contribution from the ionized gas in the A_V^{dust} determination, and (2) there is no significant contribution from foreground/background gas not associated to 30Dor and not accounted for by our PDR models. Our result not only strengthens the A_V^{max} range obtained in Section 4.4, but also suggests that this range remains valid at a resolution of 22″. While this result seems to favor the plane-parallel geometry over the spherical geometry, we wish to stress that we cannot easily derive the effective extinction corresponding to spherical clouds observed in any given pixel and that the large extinction probed at the center of the spherical cloud is not representative of this effective extinction.

Finally, we discuss the possible existence of clumps embedded in an interclump medium. Since the filling factor determined with [C II] in Section 5.1 may characterize an interclump medium surrounding small CO clumps, it is possible that the [C II] and the CO emission are not associated with the same structures. For example, a recent study of the N159 region by Okada et al. (2015) find that up to 50% of [C II] cannot be associated with the CO emission based on the velocity profiles of the lines. Testing the clumpiness of the medium would require to adopt a distribution of clouds of different sizes and pressures, illuminated by a central source and including the effect of scattering and shielding, for each pixel of the map. Unfortunately, such a scenario cannot be properly modeled yet due to the lack of observational constraints.

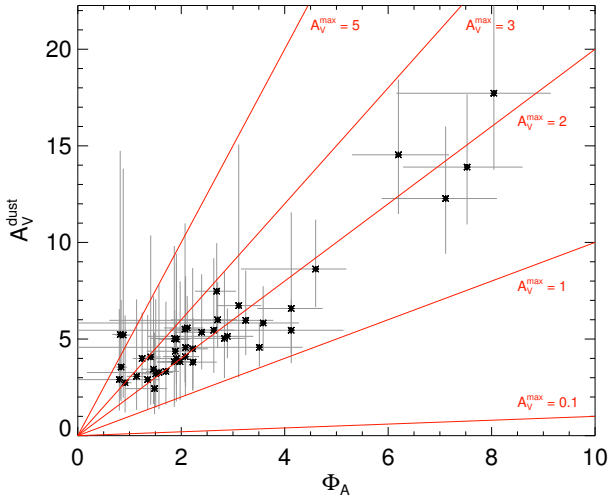

Fig. 18. The extinction derived from the dust mass A_V^{dust} is plotted against the filling factor Φ_A. The diagonal lines show different values of the extinction in individual PDR clouds (A_V^{max}). The data points agree with A_V^{dust} for $A_V^{max} \sim 1-3$.

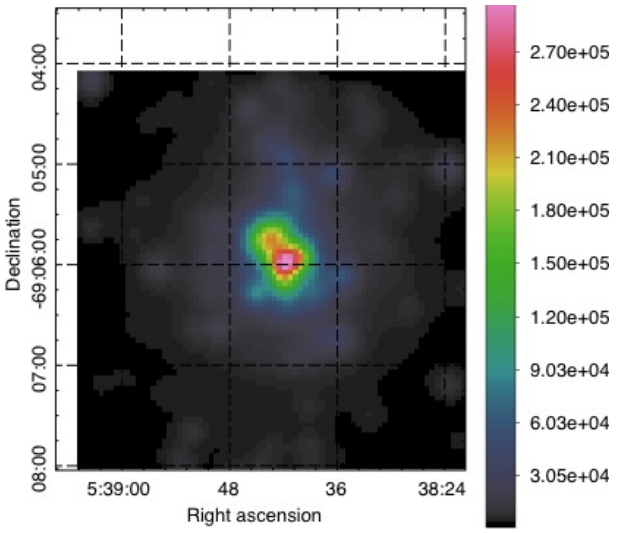

Fig. 19. Intensity of the emitted radiation field G_{stars} in the plane of R136, at 12″ resolution (color bar in units of the Mathis field).

5.3. 3D distribution of the gas

In this section we determine the physical distance between the clouds and the ionizing sources to reconstruct the 3D distribution of the gas. This is done by comparing the incident G_{UV}, predicted by the Meudon PDR code, and the emitted radiation field, G_{stars}. We define G_{stars} as the FUV radiation field computed from the known massive stellar population from the literature. We use catalogs of stars from Crowther & Dessart (1998) and Selman & Melnick (1999), including O and B stars and Wolf-Rayet (WF) stars. We use the temperature of the brightest optical sources and integrate over a blackbody between 912 and 2400 Å to be consistent with the definition of G_{UV} in the Meudon PDR code. We then use a $\frac{1}{R^2}$ relation, where R is defined as the physical distance from the center of the cluster, to calculate an average G_{stars} in each pixel of a cube centered on R136. We first make the assumption that all of the stars lay on the same plane, and derive the G_{stars} presented in Figure 19. G_{stars} is then the maximum incident radiation field we expect on each point of the cube since no absorption is taken into account.

The ratios used to constrain G_{UV} and P are independent of the filling factor, since [O I] 145 μm, [C II] and L_{FIR}^{PDR} are supposed to be almost co-spatial in the PDR model. Thus, G_{UV} determined with the model is also independent of the filling factor. In that case, the incident radiation field, G_{UV}, should be equal to the emitted radiation field G_{stars}, modulated by the distance to the R136 plane, assuming there is no absorption between the ionizing stars and the PDR (i.e. the distance to the plane calculated here is an upper limit on the actual distance). We can determine simultaneously four parameters : G_{UV}, P, Φ_A and z (the distance to the plane of R136) for each pixel of the map, using the following relations :

$$L_{FIR\ obs}^{PDR} = \Phi_A \times L_{FIR\ pred}^{PDR} \quad (2)$$

$$G_{stars} = G_{UV} \times \frac{z^2 + d^2}{d^2} \quad (3)$$

$$I_j = M_j \quad (4)$$

where d is the projected distance between a pixel and the central source, $\sqrt{z^2 + d^2} = R$. I_j are the observed values of the line intensity ratios j and M_j the ratios calculated by the PDR model (in erg s^{-1}cm^{-2}sr^{-1}). G_{UV} and G_{stars} are in units of the Mathis field. G_{UV} and P are calculated as described in Section 4.3, using Equation 4.

The physical distance R between PDR clouds and R136 is presented in Figure 20. It ranges from ~ 11 to 80 pc. The gas located close to R136 in the projected view is actually 40 to 80 pc away from the cluster. The bright arm-like structure in [O III], which, when projected, appears further from R136, is much closer to the star cluster as it is almost on the same plane. This is consistent with the distance calculated in Pellegrini et al. (2011) for the ionized gas using optical observations.

The physical distance described above was derived by assuming that all of the stars are located in the same plane. For comparison, we have also considered a random distribution of the stars in the perpendicular direction, but maintaining a high density of stars within a 6 pc radius around the center of R136 in order to reproduce a spherical distribution. We performed a Monte-Carlo simulation and calculated distances similar to our previous determination (< 40% difference throughout the map). This is not surprising as most stars in R136 are in fact located in a ~ 6 pc radius sphere. We used the Monte-Carlo simulation to estimate a typical uncertainty on the physical distance of ~ 4 pc.

5.4. Porosity of the ISM

The [O III] 88 μm line emission is detected over large spatial scales in 30Dor, as it had been already noticed in other extended sources (e.g. in N11 by Lebouteiller et al. 2012) and, together with the small scale CO clumps we see, may be indicative of a highly porous region. There is probably mixing of the ionized and neutral phases of the ISM throughout all spatial scales. This idea is supported by Figure 21, which shows the ratio [O III]/[C II] as a function of Φ_A. We can see that these two quantities are strongly correlated. Indeed, a low area filling factor Φ_A in a given pixel implies a small volume fraction occupied by PDRs. This means that there is less matter per unit volume to absorb the UV radiation, and this radiation is able to travel further away. Region B from Figure 3 (violet), at ~ 40 pc from R136, has the lowest [O III]/[C II] ratio and the highest PDR filling factor. This is also where the [C II] peaks and the CO clumps reside (see con-

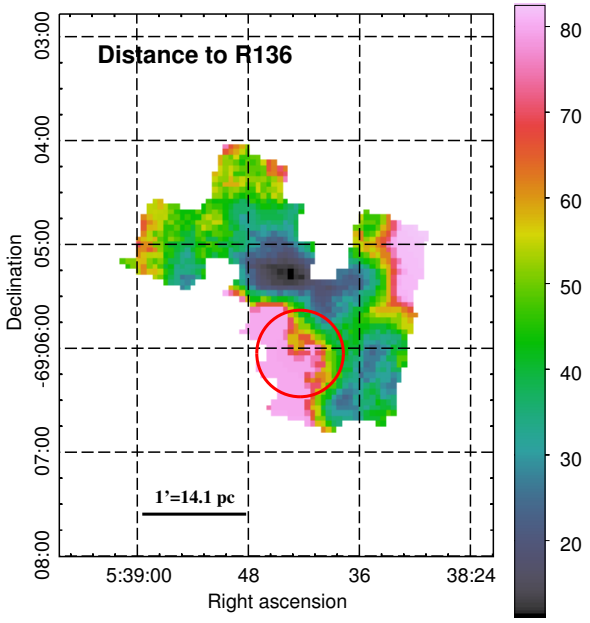

Fig. 20. Physical distance R (in pc) of the surface of the PDR to the center of R136. The red circle shows the location of R136.

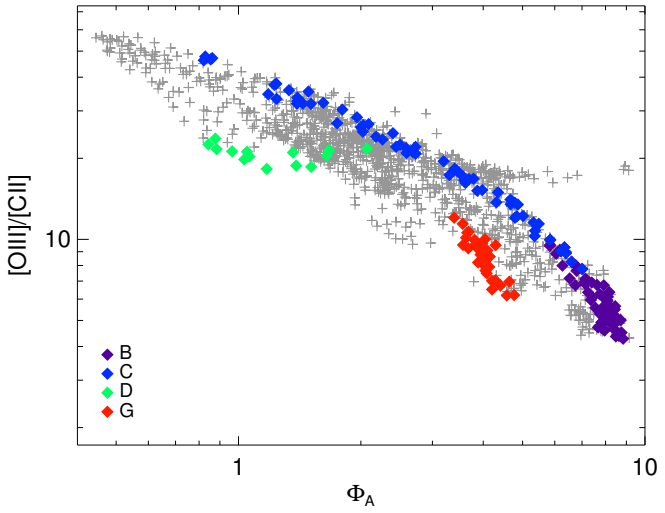

Fig. 21. Correlation between [O III]/[C II] and the PDR area filling factor. The color symbols are associated with the regions defined in Figure 3. The grey symbols are all of the other pixels of our 30Dor map.

tours in Figure 16). In contrast, the ratio [O III]/[C II] is high (> 10) in region D (green), which is one of the furthest region from R136, with a low Φ_A. The blue points of region C, which is the [O III] peak and near the G_{UV} and P peaks, show a large range of [O III]/[C II] and Φ_A. This is a region of widely varying ISM conditions. Note that the ratio [O III]/[C II] as a function of the physical distance R or G_{UV} is a scatter plot, highlighting the fact that the proximity of the ionizing source is not the only controlling factor of the structure of the ISM.

Over the mapped area of 42 pc × 56 pc the PDR filling factor and the [O III]/[C II] ratio vary over one order of magnitude. The decrease in dust abundance and intense UV photons from the SSC conspire together to shape the surrounding porous ISM, filling it with hard photons and relatively small filling factor of PDR clumps.

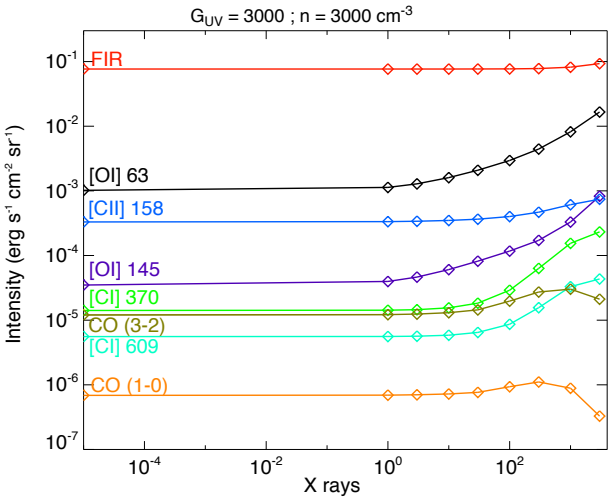

Fig. 22. Influence of the X-ray luminosity on the intensities of individual lines for a typical isochoric model with $G_{UV} = 3 \times 10^3$ and $n = 3 \times 10^3$ cm^{-3}. G_X is the X-ray luminosity integrated between 0.2 and 8 keV, given in unit of the Habing field (Habing 1968). This is to be compared with our results for G_{UV} (see Section 5.5).

5.5. Other sources of excitation

No evidence of any shock tracers has been found in 30Dor for now by previous studies (Indebetouw et al. 2009; Yeh et al. 2015). We investigate here the possibility for X-rays to be an important source of excitation of the gas in 30Dor. Townsley et al. (2006) have studied the population of X-ray point sources (energy between 0.5 and 8 keV) in a 17′ × 17′ field around R136 with *Chandra*. Spectral fitting is performed on the brightest sources (49 in total). In particular, they determine a total X-ray luminosity, corrected for the absorption, of $10^{36.95}$ erg s^{-1} for the brightest source in R136 (Mk 34), with an X-ray flux of 2×10^{-3} erg s^{-1}cm^{-2}sr^{-1} at a distance of 20 pc away, approximately at the ionization front. As presented in Figure 22, such a low G_X, compared to the values of G_{UV}, does not have an important effect on the intensity of the individual lines for a given G_{UV} and density.

5.6. If 30Dor were unresolved

Studying resolved nearby galaxies can help us understand more distant unresolved targets. At a distance of 900 kpc, the entire region of 30Dor mapped in [O I] 145 μm with PACS (covering 56 pc × 70 pc) would fall in only one spaxel of the PACS spectrometer. This distance is comparable to the distance of the Andromeda galaxy (∼780 kpc).

We integrate all of the tracers we have and perform the same study at this lower resolution, with only one pixel. Using the same technique as Section 4.3, we find that all of the [C II] emission originates from the PDRs. Using the Meudon PDR code, we determine $G_{UV} = 1390$, $P = 6.18 \times 10^5$ cm^{-3} K and $A_V = 1 - 2$. This is representative of a region of moderate G_{UV} and P in our detailed spatial study such as region G in Figure 3 or the ISM north of region B.

Even though our map is relatively small and centered on R136, the global solution is already biased toward the solution corresponding to regions with relatively low P and low G_{UV}. However, we have to keep in mind that the regions targeted with PACS are the most luminous around R136, especially for the

[O I] 145 μm line. This implies that if we were to integrate an even larger area, the result would be presumably biased even more to this diffuse and low G_{UV} regime. These two parameters could be even lower if we include more diffuse regions, which is the subject of a subsequent study in the LMC.

6. Conclusions

We have studied the ISM properties in the extreme environment of 30Dor in the LMC, around the super star cluster R136. We summarize our results as follow:

1. We have presented and analyzed new *Herschel*/PACS observations of 30Dor in [C II] 158 μm, [O I] 63 and 145 μm, [N II] 122 and 205 μm and [O III] 88 μm over a 56×70 pc region of 30Dor. All of these lines are well detected and provide diagnostics on the structure of the ISM.
   The [O III] line is the brightest of the FIR lines, ranging from 2 to 60 times more luminous than [C II]. We propose that the [O I] 63 μm line is optically thick throughout the mapped region. We find that the [C II]/CO(1-0) luminosity ranges between 5×10^4 and 3×10^5 throughout the map. This range is larger than the broad range of ratios found from integrated DGS dwarf galaxies of Cormier et al. (2014).
2. Using the *Spitzer* and *Herschel* MIR to submm photometric observations, we model the full dust SED spatially around 30Dor and derive the infrared luminosity map. We find that the [C II] intensity ranges from 0.1 to 1% of the observed L_{FIR} throughout the region mapped.
3. Based on the electron density of the ionized gas (10 to 100 cm^{-3}) and on the high value of the [C II]/[N II] ratio, we have determined that at least 90% of the [C II] emission originates from the PDRs, which makes the [C II] intensity a valuable constraint for our PDR modeling.
4. We have decomposed the L_{FIR} map to separate the component associated with the ionized gas from the PDR-only component. We find, in places, that ~ 70% of the L_{FIR} is not from PDRs, but associated with the ionized gas component, which we remove for the PDR modeling. We emphasize caution when applying the total L_{FIR} to PDR models without considering the origin of the L_{FIR}.
5. From the ratios ([O I] 145 μm+[C II])/L_{FIR}^{PDR} and [O I] 145 μm/[C II] we have determined the spatial distribution of the radiation field and the pressure with the Meudon PDR code. G_{UV} ranges between 10^2 and 3×10^4 (in units of the standard radiation field defined in Mathis et al. 1983) and P ranges between 10^5 and 1.7×10^6 cm^{-3} K.
6. The total depth of the clouds is determined by including the ratios [C II]/[C I] or [C II]/CO in the modeling assuming that all of these tracers are associated with the same structures. We showed that in the 30Dor region, A_V^{max} in 30″ pixels is ~1-3 mag. This value should be considered as a minimum value due to our assumption of a plane-parallel geometry.
7. We have conducted a 3D model of the PDR gas around R136. Comparison of the incident radiation field determined from our PDR model, G_{UV}, with the emitted radiation field, G_{stars}, reveals that the PDR gas is distributed at various distances ranging between 20 to 80 pc from the excitation source, R136.
8. The PDR area filling factor ranges between 0.6 (at the peak of G_{UV}) and 9 (at the peak of [C II]). The high value of the [O III]/[C II] ratio and its tight correlation with the filling factor rather than with the distance, highlight the porosity of the ISM, filled with hard photons around relatively small PDR clumps.

The combined effects of a half-solar metallicity gas with the intense excitation source R136 create the extreme environment we see in 30Dor. It has been shown that the structure of the gas in this region is dominated by photoionization. X-rays or shocks are not needed to reproduce the observed line intensities. Based on our findings in the present study, we speculate that the small size of the CO core inside the PDR clouds could explain the high [C II]/CO ratio we observe in low metallicity environments. The high value of the [O III] emission line suggests that a highly porous medium is a characteristic of the gas in low-metallicity dwarf galaxies.

Acknowledgements. The authors would like to thank Annie Hughes for providing the CO(1-0) data and Akiko Kawamura for the CO(3-2) data. This research was made possible through the financial support of the Agence Nationale de la Recherche (ANR) through the programme SYMPATICO (Program Blanc Projet (NR-11-BS56-0023) and also through the EU FP7. PACS has been developed by MPE (Germany); UVIE (Austria); KU Leuven, CSL, IMEC (Belgium); CEA, LAM (France); MPIA (Germany); INAFIFSI/OAA/OAP/OAT, LENS, SISSA (Italy); IAC (Spain). This development has been supported by BMVIT (Austria), ESA-PRODEX (Belgium), CEA/CNES (France), DLR (Germany), ASI/INAF (Italy), and CICYT/MCYT (Spain). SPIRE has been developed by Cardiff University (UK); Univ. Lethbridge (Canada); NAOC (China); CEA, LAM (France); IFSI, Univ. Padua (Italy); IAC (Spain); SNSB (Sweden); Imperial College London, RAL, UCL-MSSL, UKATC, Univ. Sussex (UK) and Caltech, JPL, NHSC, Univ. Colorado (USA). This development has been supported by CSA (Canada); NAOC (China); CEA, CNES, CNRS (France); ASI (Italy); MCINN (Spain); Stockholm Observatory (Sweden); STFC (UK); and NASA (USA). SPIRE has been developed by a consortium of institutes led by Cardiff Univ. (UK) and including: Univ. Lethbridge (Canada); NAOC (China); CEA, LAM (France); IFSI, Univ. Padua (Italy); IAC (Spain); Stockholm Observatory (Sweden); Imperial College London, RAL, UCL-MSSL, UKATC, Univ. Sussex (UK); and Caltech, JPL, NHSC, Univ. Colorado (USA). This development has been supported by national funding agencies: CSA (Canada); NAOC (China); CEA, CNES, CNRS (France); ASI (Italy); MCINN (Spain); SNSB (Sweden); STFC, UKSA (UK); and NASA (USA).

Appendix A: PACS observations

OBSID	Coordinates	Lines	Observation date	Exposition time (s)	Rasters nb	Mode
1342222085	5h38m35,00s -69d05m39,0s	[O III]$_{88}$, [C II]$_{158}$	740	2513,0	4	faint line
1342222086	5h38m48,00s -69d06m37,0s	[O I]$_{63}$	740	908,0	2	faint line
1342222087	5h38m58,00s -69d04m43,0s	[O I]$_{63}$	740	1322,0	4	faint line
1342222088	5h38m58,00s -69d04m43,0s	[O III]$_{88}$, [C II]$_{158}$	740	2515,0	4	faint line
1342222089	5h38m48,00s -69d06m37,0s	[O III]$_{88}$, [C II]$_{158}$	740	1703,0	2	faint line
1342222090	5h38m56,66s -69d04m56,9s	[O I]$_{145}$	740	451,0	1	faint line, pointed
1342222091	5h38m34,92s -69d06m07,0s	[N II]$_{122}$	740	452,0	1	faint line, pointed
1342222092	5h38m45,00s -69d05m23,0s	[O I]$_{63}$	740	1734,0	6	faint line
1342222093	5h38m35,00s -69d05m39,0s	[O I]$_{145}$	740	1321,0	4	faint line
1342222094	5h38m45,00s -69d05m23,0s	[O III]$_{88}$, [C II]$_{158}$	740	3325,0	6	faint line
1342222095	5h38m46,10s -69d04m58,8s	[N II]$_{122}$	740	452,0	1	faint line, pointed
1342222096	5h38m45,00s -69d05m23,0s	[O I]$_{145}$	740	1735,0	6	faint line
1342222097	5h38m35,00s -69d05m39,0s	[O I]$_{63}$	740	1320,0	4	faint line
1342231279	5h38m38,00s -69d06m00,0s	[C II]$_{158}$	889	801,0	3	bright line
1342231280	5h38m30,00s -69d06m07,0s	[O III]$_{88}$	889	724,0	3	bright line
1342231281	5h38m30,00s -69d05m07,0s	[C II]$_{158}$	889	801,0	3	bright line
1342231282	5h38m55,00s -69d03m49,0s	[O I]$_{63}$, [C II]$_{158}$	889	1133,0	2	bright line
1342231283	5h38m30,.00s -69d06m07,0s	[O I]63, [C II]$_{158}$	889	1420,0	3	bright line
1342231284	5h38m56,00s -69d04m50,0s	[N II]$_{122}$	889	662,0	2	bright line
1342231285	5h38m40,00s -69d04m38,0s	[O III]$_{88}$	889	576,0	2	bright line

Table A.1. Technical details on the observations. All of the observations were done in unchopped mode.

Appendix B: Spherical geometry

The Meudon PDR code is a plane parallel model. The code computes the abundance profiles of the various species and excited states in a plane parallel system as a function of the distance to the surface of the cloud. It is possible to post-process the results of a simulation to wrap the structure and simulate a spherical cloud. To do that, we integrate the intensity of each transition over a sphere, where the abundance profiles of each species as a function of the distance to the surface of the sphere is equal to the computed abundance profile as a function of the distance to the surface for a plane parallel geometry. The resulting line ratios as a function of the diameter of the sphere, for an integrated cloud illuminated by an isotropic field, are shown in the right panel of Figure B.1.

This is approach is geometrical. It is not done to accurately model the physics of a spherical cloud but to investigate the impact of the geometry on the integrated intensity, similar to the approach or Bolatto et al. (1999). Physically, this approach is only valid when there is enough extinction, i.e. for values of $A_V \gtrsim 5$. In addition, we wish to emphasize that the approach of computing a spherical cloud by wrapping the structure is not satisfactory in the case of clouds illuminated by a central stellar cluster since the radiation field seen by any cloud is not isotropic. The ideal model would be a model with clouds of various sizes located at various distances from a central radiation source.

References

Abel, N. P., Sarma, A. P., Troland, T. H., & Ferland, G. J. 2007, ApJ, 662, 1024
Allen, M. G., Groves, B. A., Dopita, M. A., Sutherland, R. S., & Kewley, L. J. 2008, ApJS, 178, 20
Aniano, G., Draine, B. T., Gordon, K., & Sandstrom, K. M. 2011, PASP, 123, 1218
Asplund, M., Grevesse, N., Sauval, a. J., & Scott, P. 2009, ARA&A, 47, 481
Bernard-Salas, J., Habart, E., Arab, H., et al. 2012, A&A, 538, A37
Bolatto, A., Jackson, J., & Ingalls, J. 1999, The Astrophysical Journal, 1
Bolatto, A. D., Wolfire, M., & Leroy, A. K. 2013, ARA&A, 51, 207
Brauher, J. R., Dale, D. A., & Helou, G. 2008, ApJS, 178, 280
Bron, E., Le Bourlot, J., & Le Petit, F. 2014, A&A, 569, A100
Cigan, P., Young, L., Cormier, D., et al. 2015, eprint arXiv:1509.08935
Cormier, D., Lebouteiller, V., Madden, S. C., et al. 2012, A&A, 548, 23
Cormier, D., Madden, S. C., Hony, S., et al. 2010, A&A, 518, L57
Cormier, D., Madden, S. C., Lebouteiller, V., et al. 2015, A&A, 578, A53
Cormier, D., Madden, S. C., Lebouteiller, V., et al. 2014, A&A, 564, A121
Crowther, P. a. & Dessart, L. 1998, MNRAS, 296, 622
Fazio, G. G., Hora, J. L., Allen, L. E., et al. 2004, ApJS, 154, 10
Fulton, T. R., Baluteau, J.-P., Bendo, G., et al. 2010, Proc. SPIE, 7731, 773134
Galliano, F., Hony, S., Bernard, J.-P., et al. 2011, A&A, 536, A88
Gordon, K. D., Engelbracht, C. W., Rieke, G. H., et al. 2008, ApJ, 682, 336
Habing, H. J. 1968, Bull. Astron. Inst. Netherlands, 19, 421
Hunter, D. A. 1999, in IAU Symposium, Vol. 190, New Views of the Magellanic Clouds, ed. Y.-H. Chu, N. Suntzeff, J. Hesser, & D. Bohlender, 217
Hunter, D. A., Kaufman, M., Hollenbach, D. J., et al. 2001, ApJ, 553, 121
Indebetouw, R., Brogan, C., Chen, C. H. R., et al. 2013, ApJ, 774, 73
Indebetouw, R., de Messières, G. E., Madden, S. C., et al. 2009, ApJ, 694, 32
Indriolo, N. & McCall, B. J. 2012, ApJ, 745, 91
Indriolo, N., Neufeld, D. A., Gerin, M., et al. 2015, ApJ, 800, 40
Kaufman, M. J., Wolfire, M. G., Hollenbach, D. J., & Luhman, M. L. 1999, ApJ, 527, 795
Langer, W. D., Velusamy, T., Pineda, J. L., Willacy, K., & Goldsmith, P. F. 2014, A&A, 561, A122
Le Bourlot, J., Le Petit, F., Pinto, C., Roueff, E., & Roy, F. 2012, A&A, 541, A76
Le Petit, F., Nehme, C., Le Bourlot, J., & Roueff, E. 2006, ApJS, 164, 506
Lebouteiller, V., Bernard-Salas, J., Brandl, B., et al. 2008, The Astrophysical Journal, 680, 398
Lebouteiller, V., Cormier, D., Madden, S. C., et al. 2012, A&A, 548, A91
Liseau, R., Justtanont, K., & Tielens, A. G. G. M. 2006, A&A, 446, 561
Madden, S. C., Poglitsch, A., Geis, N., Stacey, G. J., & Townes, C. H. 1997, ApJ, 483, 200
Madden, S. C., Rémy-Ruyer, A., Galametz, M., et al. 2013, PASP, 125, 600
Mathis, J. S., Mezger, P. G., & Panagia, N. 1983, A&A, 128, 212
Meixner, M., Gordon, K. D., Indebetouw, R., et al. 2006, AJ, 132, 2268
Meixner, M., Panuzzo, P., Roman-Duval, J., et al. 2013, AJ, 146, 62
Minamidani, T., Tanaka, T., Mizuno, Y., et al. 2011, AJ, 141, 73
Negishi, T., Onaka, T., Chan, K.-W., & Roellig, T. L. 2001, A&A, 375, 566
Oberst, T. E., Parshley, S. C., Nikola, T., et al. 2011, ApJ, 739, 100
Okada, Y., Requena-Torres, M. A., Güsten, R., et al. 2015, Astronomy & Astrophysics, 580, A54
Ott, S. 2010, Astronomical Data Analysis Software and Systems XIX, 434, 139
Pagel, B. E. J. 2003, in Astronomical Society of the Pacific Conference Series, Vol. 304, CNO in the Universe, ed. C. Charbonnel, D. Schaerer, & G. Meynet, 187
Pak, S., Jaffe, D. T., van Dishoeck, E. F., Johansson, L. E. B., & Booth, R. S. 1998, ApJ, 498, 735
Pellegrini, E. W., Baldwin, J. a., & Ferland, G. J. 2011, ApJ, 738, 54
Pilbratt, G. L., Riedinger, J. R., Passvogel, T., et al. 2010, A&A, 518, L1
Pineda, J. L., Langer, W. D., & Goldsmith, P. F. 2014, A&A, 570, A121
Pineda, J. L., Mizuno, N., & Röllig, M. 2012, A&A, 544, 84
Poglitsch, A., Krabbe, A., Madden, S. C., et al. 1995, ApJ, 454, 293
Poglitsch, A., Waelkens, C., Geis, N., et al. 2010, A&A, 518, L2
Rémy-Ruyer, A., Madden, S. C., Galliano, F., et al. 2014, A&A, 563, A31
Rémy-Ruyer, A., Madden, S. C., Galliano, F., et al. 2013, A&A, 557, A95
Rémy-Ruyer, A., Madden, S. C., Galliano, F., et al. 2015, Astronomy & Astrophysics, 582, A121
Rieke, G. H., Young, E. T., Engelbracht, C. W., et al. 2004, ApJS, 154, 25
Rolleston, W. R. J., Trundle, C., & Dufton, P. L. 2002, A&A, 396, 53
Röllig, M., Ossenkopf, V., Jeyakumar, S., Stutzki, J., & Sternberg, A. 2006, A&A, 451, 917
Rubio, M., Garay, G., & Probst, R. 1998, The Messenger, 93, 38
Schruba, A., Leroy, A. K., Walter, F., et al. 2012, AJ, 143, 138
Selman, F. & Melnick, J. 1999, A&A, 549, 532
Smith, J. D. T., Armus, L., Dale, D. A., et al. 2007a, PASP, 119, 1133
Smith, J. D. T., Draine, B. T., Dale, D. a., et al. 2007b, ApJ, 656, 770
Stacey, G. J., Geis, N., & Genzel, R. 1991, ApJ, 373, 423
Stacey, G. J., Hailey-Dunsheath, S., Ferkinhoff, C., et al. 2010, ApJ, 724, 957
Swinyard, B. M., Polehampton, E. T., Hopwood, R., et al. 2013, MNRAS, 440, 3658
Tielens, a. G. G. M. & Hollenbach, D. 1985, ApJ, 291, 722
Townsley, L. K., Broos, P. S., Feigelson, E. D., et al. 2006, AJ, 131, 2140
Walker, A. R. 2012, Astrophysics and Space Science, 341, 43
Werner, M. W. W., Roellig, T. L. L., Low, F. J. J., et al. 2004, ApJS, 154, 1
Wolfire, M. G., Hollenbach, D., & McKee, C. F. 2010, ApJ, 716, 1191
Wolfire, M. G., Tielens, A. G. G. M., & Hollenbach, D. J. 1990, ApJ, 358, 116
Wong, T., Hughes, A., Ott, J., et al. 2011, ApJS, 197, 16
Wu, R., Madden, S. C., Galliano, F., et al. 2015, A&A, 575, A88
Wu, R., Polehampton, E. T., Etxaluze, M., et al. 2013, A&A, 556, A116
Yeh, S. C. C., Seaquist, E. R., Matzner, C. D., & Pellegrini, E. W. 2015, ApJ, 807, 117

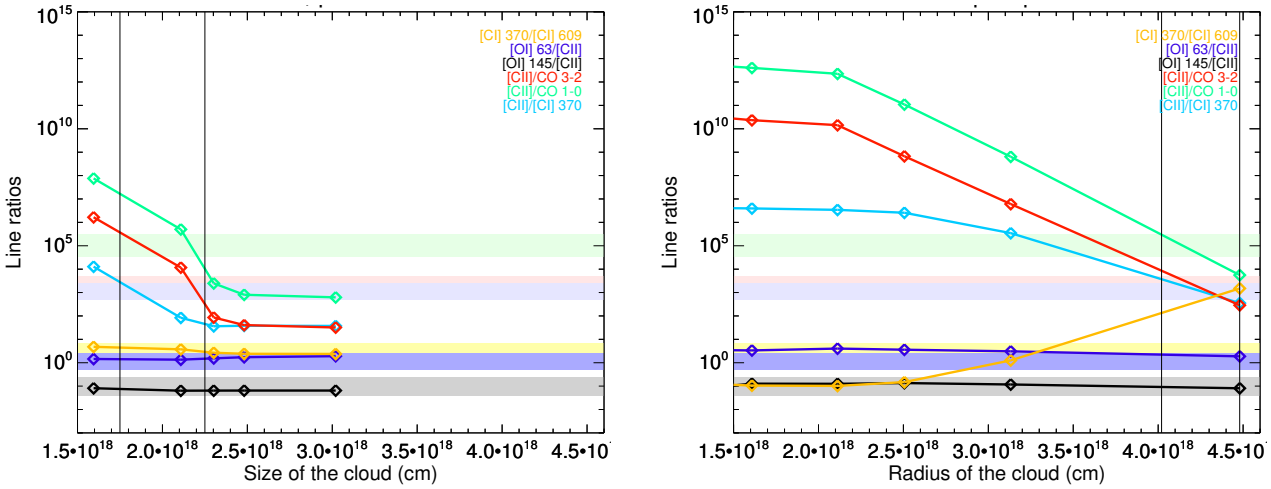

Fig. B.1. *Left:* Ratios $\mathcal{R}$ of the modeled line ratios for [C I] 370 μm/[C I] 609 μm, [O I] 63 μm/[C II], [O I] 145 μm/[C II], [C II]/CO(3-2), [C II]/ CO(1-0) and [C II]/ [C I]370 μm, for simulated plane parallel clouds of different sizes, with G_{UV} = 1 × 10^3 and P = 3 × 10^5 cm^{-3} K. *Right:* Same for spherical clouds of different radius. The vertical lines indicate the range of radius where the predictions of the model are compatible with the observed [C II]/ CO(3-2) and [C II]/ [C I]370 μm.